nature genetics

ARTICLES

https://doi.org/10.1038/s41588-021-00820-3

H2AK119ub1 guides maternal inheritance and zygotic deposition of H3K27me3 in mouse embryos

Hailiang Mei[1,6], Chisayo Kozuka[1], Ryoya Hayashi[1,2], Mami Kumon[1], Haruhiko Koseki[3,4,5] and Azusa Inoue[1,2,6] ✉

Parental epigenomes are established during gametogenesis. While they are largely reset after fertilization, broad domains of Polycomb repressive complex 2 (PRC2)-mediated formation of lysine 27-trimethylated histone H3 (H3K27me3) are inherited from oocytes in mice. How maternal H3K27me3 is established and inherited by embryos remains elusive. Here, we show that PRC1-mediated formation of lysine 119-monoubiquititinated histone H2A (H2AK119ub1) confers maternally heritable H3K27me3. Temporal profiling of H2AK119ub1 dynamics revealed that atypically broad H2AK119ub1 domains are established, along with H3K27me3, during oocyte growth. From the two-cell stage, H2AK119ub1 is progressively deposited at typical Polycomb targets and precedes H3K27me3. Reduction of H2AK119ub1 by depletion of Polycomb group ring finger 1 (PCGF1) and PCGF6—essential components of variant PRC1 (vPRC1)—leads to H3K27me3 loss at a subset of genes in oocytes. The gene-selective H3K27me3 deficiency is irreversibly inherited by embryos, causing loss of maternal H3K27me3-dependent imprinting, embryonic sublethality and placental enlargement at term. Collectively, our study unveils preceding dynamics of H2AK119ub1 over H3K27me3 at the maternal-to-zygotic transition, and identifies PCGF1/6-vPRC1 as an essential player in maternal epigenetic inheritance.

The maternal and paternal genomes are packaged in very different chromatin configurations in mammalian gametes. Consequently, totipotent zygotes exhibit parental asymmetry in various epigenetic features, including histone post-translational modifications (PTMs), histone variants, DNA methylation, chromatin accessibility and higher-order chromatin structures[1–12]. Although the parental asymmetry is largely resolved after fertilization, owing to extensive reprogramming[13–21], DNA methylation at imprinting control regions and oocyte-derived H3K27me3 can escape such reprogramming and regulate parental allele-specific imprinted gene expression[18,22–24]. Maternal inheritance of H3K27me3 causes paternal allele-specific expression of dozens of genes in a DNA-methylation-independent manner in mouse preimplantation embryos[25–28]. This maternal H3K27me3-dependent imprinting is taken over by secondary DNA methylation in extraembryonic cells of postimplantation embryos to regulate placenta-specific imprinting[29,30]. Remarkably, various organisms, including nematodes, flies and plants, also adopt an analogous mechanism of embryonic gene regulation by maternally inherited H3K27me3 (refs. [31–34]). These studies raise intriguing questions of how maternally heritable H3K27me3 is established in oocytes and maintained in embryos and what its long-term functions are.

Polycomb repressive complex 2 (PRC2)-mediated H3K27me3 formation interplays with PRC1-mediated H2AK119ub1 formation to coordinate the formation of repressive Polycomb domains in embryonic stem cells (ESCs). Yet, how they function in vivo remains poorly understood. Although H2AK119ub1 was previously thought to be downstream of H3K27me3, recent studies have revisited this assumption[35–38]. The essential core of PRC1 consists of an E3 ubiquitin ligase, RING1A or RING1B. PRC1 exists in six different forms (PRC1.1 to PRC1.6), which contain one of the six Polycomb group ring finger (PCGF) proteins (PCGF1 to PCGF6, respectively) essential for PRC1 functions[39]. Among these, the variant PRC1 (vPRC1) proteins (PRC1.1, PRC1.3, PRC1.5 and PRC1.6), but not canonical PRC1 (cPRC1) proteins (PRC1.2 and PRC1.4), have high catalytic activity for H2AK119ub1 deposition[40,41]. Genetic perturbation experiments in ESCs have shown that PRC1 can be recruited to Polycomb targets even in the absence of PRC2, and that depletion of H2AK119ub1 or vPRC1 causes loss of H3K27me3 (refs. [40,42–49]). In mouse embryos, PCGF3/5 depletion causes failure in H3K27me3 accumulation at inactive X chromosomes[45,50]. These studies collectively indicate that vPRC1-mediated H2AK119ub1 can act upstream of H3K27me3. However, because of the difficulty in mapping H2AK119ub1 for in vivo small-scale samples, it remains unknown how H2AK119ub1 is spatiotemporally regulated and whether it is coordinated with H3K27me3 in a physiological context.

To address these questions, here, we applied low-input cleavage under targets and release using nuclease (CUT&RUN)[51] to profile H2AK119ub1 dynamics during mouse oogenesis and early embryogenesis, and investigated the roles of H2AK119ub1 in maternal inheritance of H3K27me3.

Results

Establishment of H2AK119ub1 during oocyte growth. H3K27me3 forms a broad and distal-rich (noncanonical) distribution in mouse

[1]YCI Laboratory for Metabolic Epigenetics, RIKEN Center for Integrative Medical Sciences, Yokohama, Japan. [2]Tokyo Metropolitan University, Hachioji, Japan. [3]Laboratory for Developmental Genetics, RIKEN Center for Integrative Medical Sciences, Yokohama, Japan. [4]AMED-CREST, Yokohama, Japan. [5]Cellular and Molecular Medicine, Advanced Research Departments, Graduate School of Medicine, Chiba University, Chiba, Japan. [6]These authors contributed equally: Hailiang Mei, Azusa Inoue. ✉e-mail: azusa.inoue@riken.jp

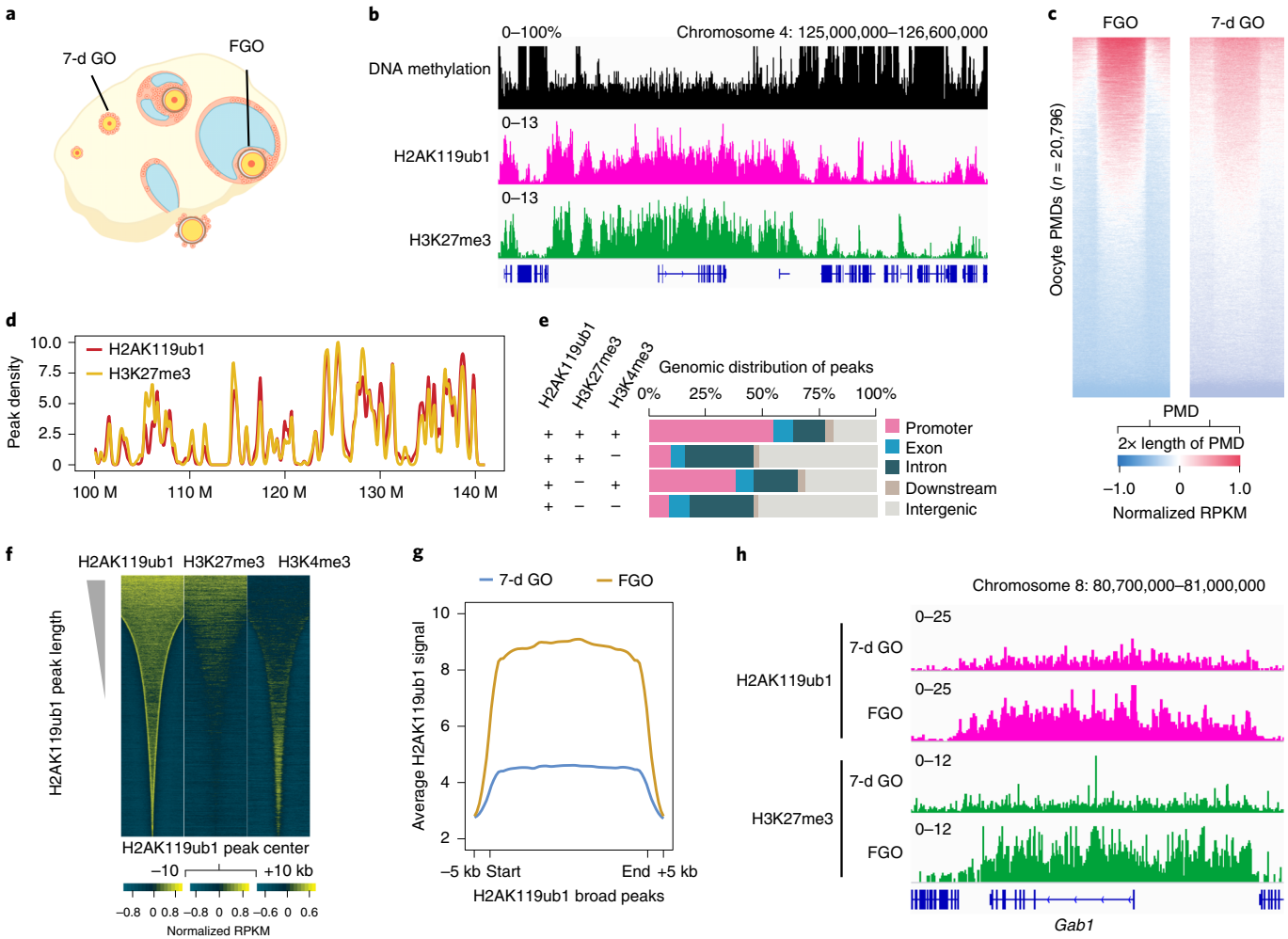

Fig. 1 | H2AK119ub1 is established in a noncanonical distribution along with H3K27me3 in mouse oocytes. a, Illustration of a 7-d GO and an FGO in an ovary. **b**, Genome browser view of H2AK119ub1 distribution in FGOs. The DNA methylation and H3K27me3 ChIP-seq datasets are from ref. [19]. The scales of the tracks are indicated on the left of each track. **c**, Heatmaps showing the enrichment of H2AK119ub1 at PMDs in FGOs and 7-d GOs. Each row represents a PMD and its flanking 0.5× the PMD length both up- and downstream. **d**, General view of H2AK119ub1 and H3K27me3 peak densities along chromosome 4 (100–140 M) in FGOs. **e**, Genomic distribution of regions with the indicated histone modifications. Promoters represent the regions of ±2.5 kb around transcription start sites. **f**, Heatmap showing the enrichment of H2AK119ub1, H3K27me3 and H3K4me3 at all H2AK119ub1 peaks in FGOs. A H2AK119ub1 peak is centered and its ±10 kb flanking region is shown in each row. The rows are ordered by H2AK119ub1 peak length. The H3K27me3 and H3K4me3 ChIP-seq datasets are from ref. [19]. **g**, Average signal profiles of H2AK119ub1 at H2AK119ub1 broad peaks (peak length ≥ 10 kb) called in FGOs, and its ±5 kb flanking regions. **h**, Genome browser view of H2AK119ub1 and H3K27me3 distributions in 7-d GOs and FGOs. The H3K27me3 ChIP-seq datasets are from ref. [18].

fully grown oocytes (FGOs)[5,18]. After validating the reproducibility and quality of H2AK119ub1 low-input CUT&RUN, we applied it for FGOs (Fig. 1a and Extended Data Fig. 1a–c). We found that H2AK119ub1 is pervasively distributed within partially methylated domains (PMDs), along with H3K27me3 (Fig. 1b–d)[16]. Closer examination showed that, while broad peaks of H2AK119ub1 are associated with H3K27me3 mainly at distal (nonpromoter) regions, narrow peaks are associated with H3K4me3 preferentially at promoters (Fig. 1e,f and Extended Data Fig. 1d,e). Association between H2AK119ub1 and H3K4me3 at promoters was reminiscent of the other biological contexts reported previously[52–55]. Analysis of RNA sequencing (RNA-seq) datasets in FGOs showed that genes with H2AK119ub1/H3K27me3 are silenced, those with H2AK119ub1/H3K4me3 are highly expressed, and those with all three modifications are poorly expressed (Extended Data Fig. 1f,g), implying that H2AK119ub1 alone does not serve as a direct indicator of gene expression. It is unlikely that local H2AK119ub1 at active gene promoters plays an important role in gene regulation in oocytes, because genes harboring promoter H2AK119ub1/H3K4me3 are not severely dysregulated in *Ring1a/1b* knockout (KO) FGOs that lack H2AK119ub1 (Extended Data Fig. 1h)[56,57]. Taken together, these data show that H2AK119ub1 coexists with H3K27me3 in a noncanonical distribution, while it is also associated with H3K4me3 at active gene promoters in FGOs.

Noncanonically broad H3K27me3 is established during oocyte growth[18]. To determine whether this is also the case for H2AK119ub1, we performed H2AK119ub1 CUT&RUN in growing oocytes of 7-d-old females (7-d GOs) (Extended Data Fig. 1i). Comparative analysis revealed that H2AK119ub1 signals of 7-d GOs are lower than those of FGOs within broad H2AK119ub1 domains (Fig. 1g,h and Extended Data Fig. 1j). Consistently, H2AK119ub1 signals in 7-d GOs were not clearly confined within PMDs (Fig. 1c). These data suggest that the noncanonical distribution of H2AK119ub1 and H3K27me3 is co-established during oocyte growth.

H2AK119ub1 remodeling precedes H3K27me3 after fertilization. To determine the temporal dynamics of H2AK119ub1 at the maternal-to-zygotic transition, we performed H2AK119ub1 CUT&RUN for metaphase of meiosis II (MII)-stage oocytes, pronuclear stage 5 (PN5) zygotes, early two-cell-stage embryos (before major zygotic genome activation), late two-cell-stage embryos (after major zygotic genome activation), and morula and blastocyst embryos (Fig. 2a and Extended Data Fig. 2a). The total numbers of paternal and maternal allelic reads were almost comparable, except at the one-cell stage, which had a maternal allele bias (Extended Data Fig. 2b). We noted that H2AK119ub1 at the paternal genome of zygotes preferentially resides within gene desert regions, resulting in genome-wide parental asymmetry (Fig. 2b and Extended Data Fig. 2c). This was reminiscent of immunofluorescence analyses demonstrating that PRC1 and H2AK119ub1 are deposited onto the 4′,6-diamidino-2-phenylindole (DAPI)-dense paternal heterochromatin shortly after fertilization[58–60]. Our immunofluorescence analysis confirmed that H2AK119ub1 is undetectable in paternal chromatin until 1 h after fertilization (Extended Data Fig. 2d,e), suggesting that H2AK119ub1 at the paternal gene deserts is newly acquired after fertilization.

Hierarchical clustering analysis of H2AK119ub1 distribution showed a high similarity between the MII oocytes and the maternal allele of zygotes (Fig. 2b,c). Pearson correlation analysis also demonstrated that H2AK119ub1 and H3K27me3 distributions are highly correlated in both MII oocytes and one-cell zygotes (Fig. 2b,d). These data imply that maternal H2AK119ub1 and H3K27me3 are cotransmitted to zygotes. After the one-cell stage, however, H2AK119ub1, but not H3K27me3, started to be remodeled genome wide in both alleles, resulting in lower correlations between them (Fig. 2b,d). The parental asymmetry of H2AK119ub1, but not H3K27me3, was globally lost until the late two-cell stage (Fig. 2b,c), suggesting the presence of de novo catalytic activity of PRC1, but not PRC2, in two-cell embryos. The H2AK119ub1 remodeling was also evident in a gradual reduction of the intergenic peak proportions on both alleles (Extended Data Fig. 2f), which was known to occur for H3K27me3 after the blastocyst stage[18]. Indeed, H2AK119ub1 distributions in morula and blastocyst embryos resembled those in mouse ESCs (mESCs) (Fig. 2b,c) and were well correlated with H3K27me3 distributions in postimplantation epiblasts and mESCs (Fig. 2b,d). These profiles demonstrate that H2AK119ub1 is globally remodeled from the early two-cell stage towards an ESC-like canonical pattern in a manner before that of H3K27me3.

To characterize the detailed dynamics of H2AK119ub1 and H3K27me3 during the maternal-to-zygotic transition, we grouped all maternal H2AK119ub1 peaks into three clusters according to their dynamics (Fig. 3a). In cluster 1, enrichment of maternal H2AK119ub1 persisted throughout preimplantation development. This cluster possessed the strongest H3K27me3 signals from MII oocytes to blastocysts (Fig. 3a,b), suggesting that H2AK119ub1 and H3K27me3 keep their association at maternally transmitting H3K27me3 domains. In cluster 2, which had low gene density, the H2AK119ub1 enrichment was greatly decreased by the morula stage, as was the H3K27me3 from the blastocyst stage (Fig. 3a and Extended Data Fig. 3a), suggesting that loss of H2AK119ub1 precedes that of H3K27me3 at gene deserts that contain few CpG islands, the docking sites of vPRC1 (ref. [36]). Interestingly, the H2AK119ub1 enrichment at cluster 3 was progressively apparent from the early two-cell stage, which clearly preceded the emergence of H3K27me3 that occurred during or after the blastocyst stage (Fig. 3a,c). Cluster 3 was relatively enriched at promoters and had higher CpG density, indicative of an ESC-like canonical distribution[5,18] (Fig. 3a,d,e). These results indicate that both loss and gain of H2AK119ub1 precede those of H3K27me3 during the maternal-to-zygotic transition.

To characterize H2AK119ub1 dynamics at the gene level, we next grouped all gene promoters containing single-nucleotide polymorphisms (SNPs) into three clusters according to H2AK119ub1 dynamics (Extended Data Fig. 3b). Integrative analysis with RNA-seq datasets revealed that H2AK119ub1 mostly persists at transcriptionally silenced genes that are strongly enriched with maternally transmitted H3K27me3 (group A). Since maternal H3K27me3 coats gene bodies[18], we conducted the same analyses for all gene bodies and obtained a similar result (Extended Data Fig. 3c). We confirmed that group A contains almost entirely of 76 putative H3K27me3-dependent imprinted genes identified previously[27] (Fig. 3f and Extended Data Fig. 3d). Zygotic H2AK119ub1 was deposited at weakly expressed genes in a manner preceding H3K27me3 deposition initiated at the blastocyst stage (group B; Extended Data Fig. 3b). The H3K27me3 signals in some of the group B genes dropped at the one-cell stage (Extended Data Fig. 3b), a finding reminiscent of a previous observation that H3K27me3 at some typical Polycomb target genes is lost after fertilization[18]. Consistently, group B included the majority of typical Polycomb target genes defined in mESCs (Extended Data Fig. 3e,f). These data suggest that H2AK119ub1 primes zygotic Polycomb domain formation during early embryogenesis (Fig. 3g).

H3K27me3 is gene selectively lost in PCGF1/6 KO oocytes. The H2AK119ub1 dynamics led us to hypothesize that H2AK119ub1 contributes to the establishment and/or maintenance of H3K27me3 in oocytes and early preimplantation embryos. To test this, we attempted to deplete H2AK119ub1 in FGOs. However, depletion of RING1A/1B, the E3 ubiquitin ligase of PRC1, was known to cause severe developmental arrest at the one- or two-cell stage[57], preventing the study of its impact on embryonic gene regulation. We therefore aimed to deplete vPRC1 forms in oocytes. Based on RNA-seq datasets[16], the expression levels of *Pcgf1* and *Pcgf6* were high (reads per kilobase of transcript per million mapped reads (RPKM) > 300 and >50, respectively) throughout oocyte growth, while those of *Pcgf3* and *Pcgf5* were low (RPKM < 10) (Extended Data Fig. 4a). Considering the partially redundant functions of PCGF1 and PCGF6 in mESCs[41], we generated an oocyte-specific *Pcgf1* and *Pcgf6* double KO by crossing *Pcgf1* flox[45], *Pcgf6* flox and oocyte-specific *Zp3* promoter-driven *Cre* ($Zp3^{Cre}$) mouse lines[61] (Extended Data Fig. 4b–e). Herein, oocytes from $Zp3^{Cre}/Pcgf1^{fl/fl}/Pcgf6^{fl/fl}$ and $Pcgf1^{fl/fl}/Pcgf6^{fl/fl}$ females are designated as *Pcgf1/6* KO and control oocytes, respectively.

Immunofluorescence analysis revealed that the H2AK119ub1 level in KO FGOs is remarkably lower than that in control oocytes (Fig. 4a,b). Quantitative CUT&RUN analysis of H2AK119ub1 confirmed global reduction of H2AK119ub1 in KO FGOs (Fig. 4c,d and Extended Data Fig. 5a,b). Interestingly, both immunofluorescence and CUT&RUN analyses found that H3K27me3 levels are only modestly decreased in KO FGOs (Fig. 4a–d and Extended Data Fig. 5c,d). A closer examination revealed that a subset of genes lose H3K27me3: among 12,095 genes harboring H3K27me3 at their gene bodies, 747 (6.2%), 1,533 (12.7%) and 9,815 (81.1%) showed strong (fold change > 4), modest (2 < fold change < 4) and little reduction (fold change < 2) of H3K27me3, respectively (Fig. 4e,f and Supplementary Table 1). RNA-seq analysis revealed that the genes that lost H3K27me3 genes tended to be upregulated (Fig. 4e,f, Extended Data Fig. 5e and Supplementary Table 2). Notably, comparative analysis with an RNA-seq dataset of *Ring1a/1b* KO FGOs[56] indicated that both the gene number and the extent of derepression in *Pcgf1/6* KO FGOs were much lower than those in *Ring1a/1b* KO FGOs, despite significant overlap of upregulated genes (Fig. 4g–i). This finding was similar to those in a previous study showing that different PRC1 forms synergistically function in gene silencing in mESCs[41,62] and suggested that canonical PRC1 (cPRC1) and/or weakly expressed PCGF3/5 compensate for gene repression in

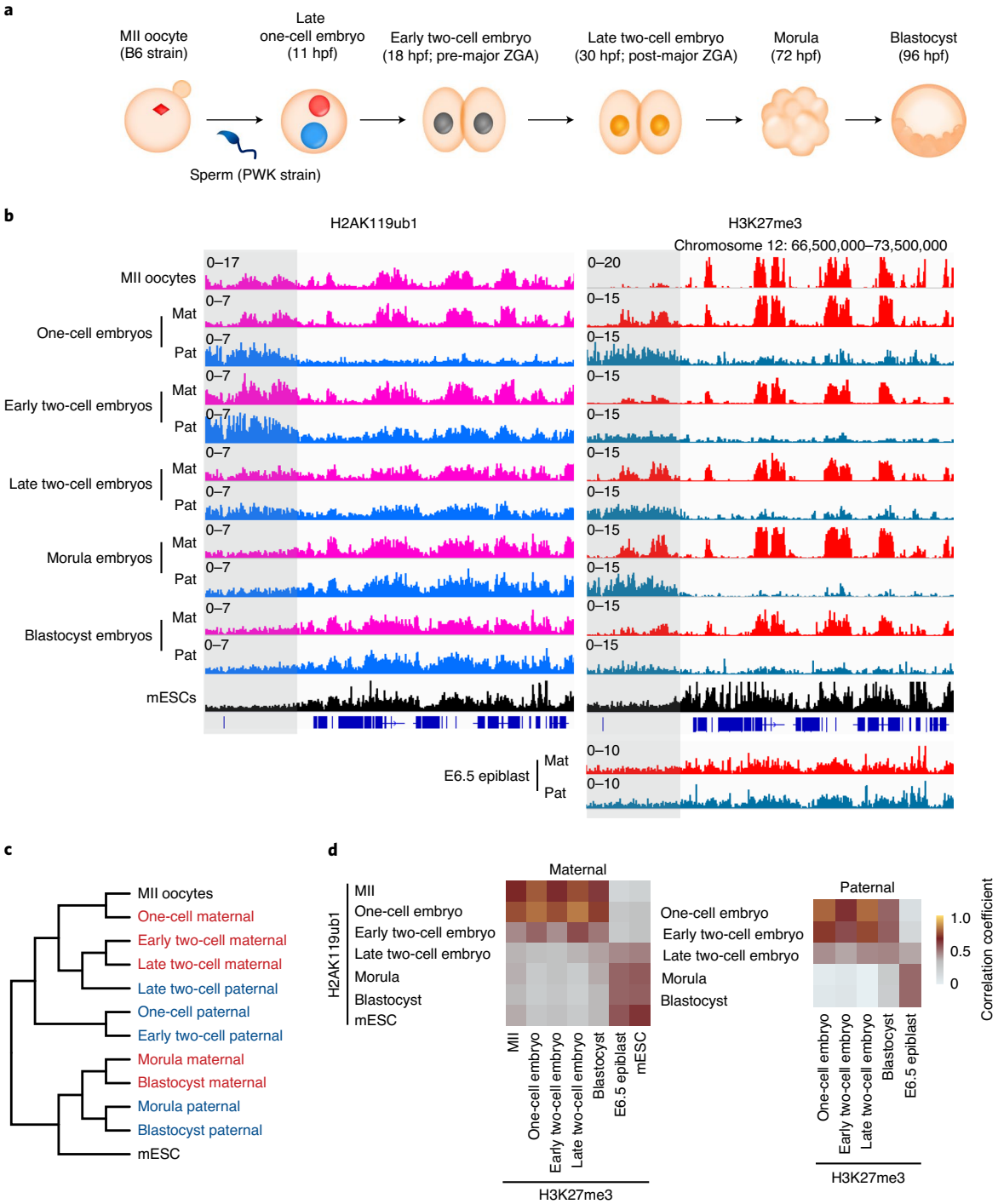

Fig. 2 | Remodeling of H2AK119ub1 precedes that of H3K27me3. a, Illustration of the oocytes and preimplantation embryos examined in this study. hpf, hours postfertilization; ZGA, zygotic genome activation. Embryos were F_1 hybrids composed of the C57/BL6 (B6) maternal genome and PWK/PhJ (PWK) paternal genome, which allows distinguishing between the parental alleles using SNP information. **b**, Genome browser views of H2AK119ub1 and H3K27me3 landscapes in MII oocytes, one-cell embryos, early two-cell embryos, late two-cell embryos, morula embryos, blastocyst embryos and mESCs. Mat, maternal allele; Pat, paternal allele. Gene desert regions (≤1 gene per Mb of window) are shaded. The H3K27me3 ChIP-seq datasets of MII oocytes are from ref. [13]; those of one-cell, early two-cell, late two-cell and blastocyst embryos, as well as E6.5 epiblasts, are from ref. [18]; the H3K27me3 CUT&RUN datasets of morulae are from ref. [26]; and the H2AK119ub1 and H3K27me3 ChIP-seq datasets of mESCs are from ref. [76]. **c**, Hierarchical clustering analysis of allelic H2AK119ub1 distributions (5-kb window). **d**, Heatmap showing pairwise Pearson correlations between H2AK119ub1 and H3K27me3 distributions in the indicated developmental stages. The H3K27me3 ChIP-seq datasets are from ref. [18].

Pcgf1/6 KO FGOs. Thus, these results show that PCGF1/6 deficiency causes gene-selective loss of H3K27me3, accompanied by modest gene derepression in FGOs.

To gain insight into the mechanisms underlying the gene-selective loss of H3K27me3, we first asked whether genes that have lost H3K27me3 are the specific targets of PRC1.6, which

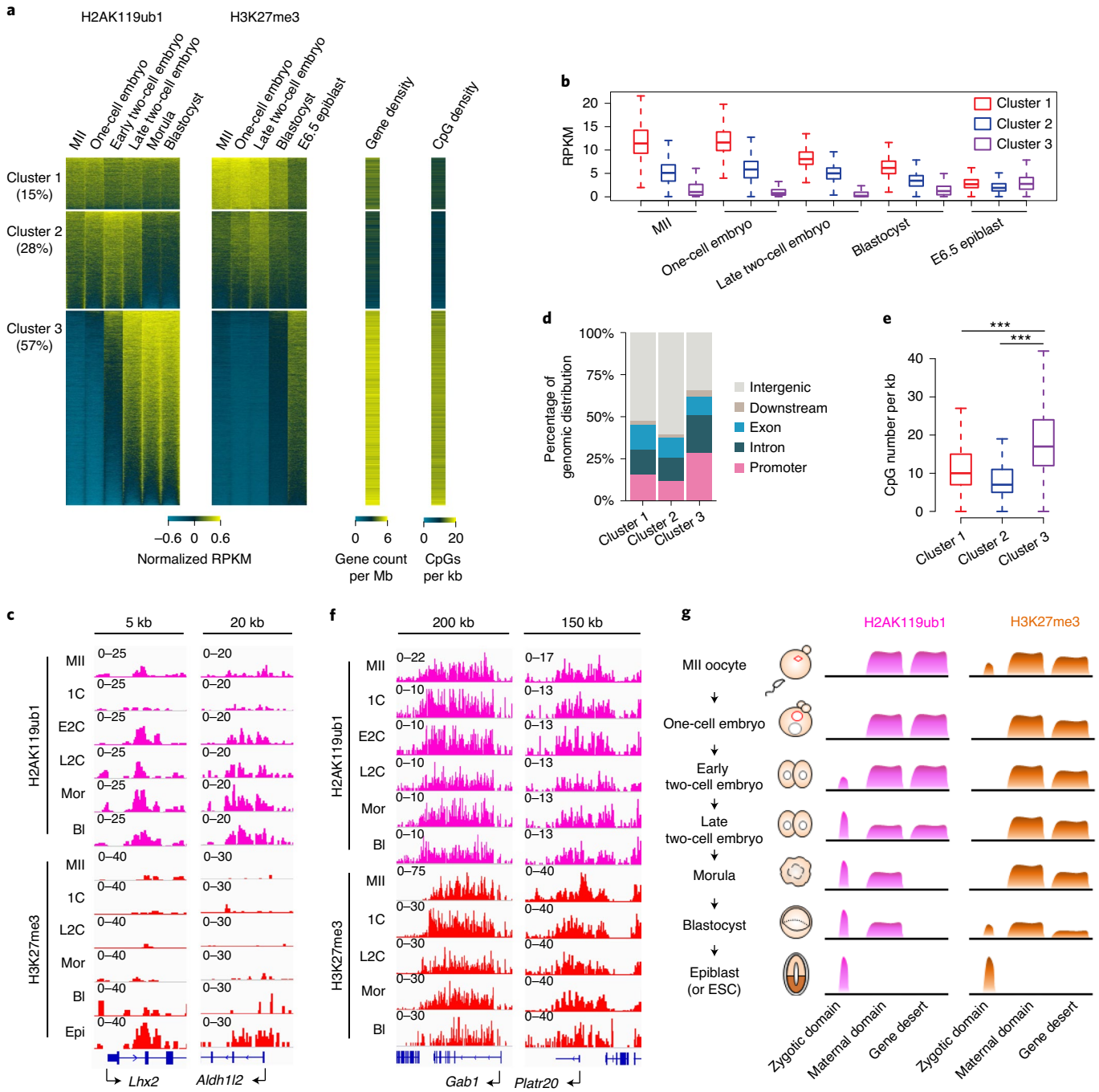

Fig. 3 | Cotransmission of maternal Polycomb domains and sequential establishment of zygotic Polycomb domains. a, Heatmap showing maternal H2AK119ub1 and H3K27me3 enrichment at all H2AK119ub1 peaks detected in at least one of the indicated samples. Clusters 1, 2 and 3 represent peak regions where H2AK119ub1 enrichment was retained, lost or gained, respectively. The gene density surrounding the H2AK119ub1 peaks and the CpG density within H2AK119ub1 peaks are shown in the two right columns. The H3K27me3 ChIP-seq datasets are from ref. [18]. **b**, Box plots showing the H3K27me3 signal intensity within H2AK119ub1 peaks of the three clusters. The center lines in the boxes represent median values. The box edges, upper and lower whiskers indicate the interquartile range (IQR; from the 25th to 75th percentile), the largest value smaller than 1.5× the IQR above the 75th percentile and the smallest value larger than 1.5× the IQR below the 25th percentile, respectively ($n=1$ as biological replicates were combined). **c**, Representative genome browser views showing maternal H2AK119ub1 and H3K27me3 dynamics at cluster 3. The genomic length of each view is indicated at the top. 1C, one-cell embryo; Bl, blastocyst; E2C, early two-cell embryo; Epi, E6.5 epiblast; L2C, late two-cell embryo; MII, MII oocyte; Mor, morula. **d**, Genomic distribution of the three clusters. Promoters represent the regions of ±2.5 kb around transcription start sites. **e**, Box plots showing the CpG densities of the three clusters. The definitions of lines, box edges and whiskers are the same as in **b** ($n=1$). $^{***}P < 2.2\times10^{-16}$ (two-sided Mann–Whitney *U*-test). **f**, Representative genome browser views showing maternal H2AK119ub1 and H3K27me3 dynamics at H3K27me3-dependent imprinted genes. **g**, Schematic of the temporal dynamics of H2AK119ub1 and H3K27me3 during the maternal-to-zygotic transition. Zygotic domain represents zygotically established Polycomb domains at which deposition of H2AK119ub1 precedes that of H3K27me3. Maternal domain represents noncanonically broad maternal Polycomb domains, except those located within gene deserts from which H2AK119ub1 loss precedes H3K27me3 loss.

contains unique transcription factors as its subunits[52,63,64]. To this end, we generated *Pcgf1* and *Pcgf6* single KO FGOs, respectively. H3K27me3 CUT&RUN revealed that only a small number of genes ($n=67$) lose H3K27me3 exclusively in *Pcgf6* KO FGOs (Fig. 4j,k, Extended Data Fig. 5f and Supplementary Table 3), indicating that the target specificity of PRC1.6 only partly accounts for the gene selectivity of H3K27me3 loss in *Pcgf1/6* KO FGOs. In contrast, H3K27me3 was more pervasively lost in *Pcgf1* KO than in *Pcgf6* KO FGOs, although the extent of H3K27me3 loss in *Pcgf1* KO FGOs was milder than that in *Pcgf1/6* KO FGOs (Fig. 4j,k). This supports the notion that PRC1.6 indeed has compensatory functions for PRC1.1. Analysis of public PCGF1 chromatin immunoprecipitation sequencing (ChIP-seq) datasets in mESCs[41] demonstrated that PCGF1 binding at promoters is more apparent in genes that have lost H3K27me3 (Extended Data Fig. 5g). Consistent with the fact that PRC1.1 preferentially binds to CpG islands[36,65], the CpG density at promoters of genes that had lost H3K27me3 was higher than that of genes with unchanged H3K27me3 (Extended Data Fig. 5h). These data suggest that the binding preference of PCGF1 contributes to the gene selectivity of H3K27me3 loss. Another possibility is that genes with unchanged H3K27me3 acquire H3K27me3 and H2AK119ub1 at a very early phase of oocyte growth, which may have prevented study of the impact on H3K27me3 establishment via the $Zp3^{Cre}$-mediated KO approach. In support of this idea, the signal intensity of H3K27me3 in genes with unchanged H3K27me3 was significantly higher than that of genes with lost H3K27me3 in 7-d GOs (Extended Data Fig. 5i). This observation did not rule out the possibility that the effect of PCGF1/6 depletion in H3K27me3 establishment is underestimated in this KO approach. Taken together, these data suggest that the target preference of PCGF1/6–PRC1 and the timing of H3K27me3 establishment would account for the gene-selective loss of H3K27me3 in *Pcgf1/6* KO FGOs.

H3K27me3 loss caused by maternal PCGF1/6 deficiency is inherited by embryos. To study how maternal PCGF1/6 deficiency affects gene regulation in embryos, we generated *Pcgf1/6* maternal KO (matKO) embryos by fertilizing KO oocytes and wild-type sperm. The numbers of MII oocytes obtained and the ratio of development to the two-cell stage were comparable between control and matKO embryos (Extended Data Fig. 6a–c). Due to developmental delay after the two-cell stage in about half of the matKO embryos for unknown reasons, the ratio of matKO embryos that reached the blastocyst stage in a timely fashion was significantly lower than that of control embryos (Extended Data Fig. 6b,c). Nevertheless, this early developmental phenotype was much less pronounced than that in *Ring1a/1b* matKO embryos[57], consistent with the milder gene derepression in *Pcg1/6* KO FGOs. For the following experiments that used matKO preimplantation embryos, we only selected those that reached the indicated stages in a timely fashion.

We then went on to examine the postfertilization dynamics of H2AK119ub1 and H3K27me3 by immunofluorescence analysis. The H2AK119ub1 signals of matKO embryos were significantly lower than those of control embryos until the four-cell stage, but then recovered by the morula stage (Fig. 5a and Extended Data Fig. 6d), possibly due to the wild-type paternal allele and/or zygotically expressed PCGF5 (Extended Data Fig. 4a). H3K27me3 signals of matKO embryos were initially comparable to those of control embryos at the early one-cell stage, but became significantly lower than those of controls by the late one-cell stage (Fig. 5a and Extended Data Fig. 6d). The H3K27me3 levels of matKO embryos remained lower than those of control embryos until the four-cell stage and then recovered by the morula stage. These results demonstrate that maternal deficiency of PCGF1/6 causes transient reduction of H3K27me3 in early preimplantation embryos.

Having demonstrated that PCGF1/6 deficiency causes gene-selective loss of H3K27me3 in FGOs, we examined whether it causes loss of maternal H3K27me3-dependent imprinting. To this end, we first defined 16 H3K27me3-dependent paternally expressed genes (PEGs) and five DNA-methylation-dependent PEGs in morula embryos by integrative analysis of RNA-seq datasets of a reciprocal cross of B6×PWK and PWK×B6 (Extended Data Fig. 7a and Supplementary Table 4), *Eed* matKO[26] and *Dnmt3* matKO embryos[29] (Fig. 5b). Next, we performed RNA-seq analysis of F_1 hybrid *Pcgf1/6* control and matKO morula embryos (Extended Data Fig. 7b and Supplementary Tables 4 and 5) and found that nine of the 16 H3K27me3-dependent PEGs, but none of the DNA-methylation-dependent PEGs, lost their allelic expression biases in *Pcgf1/6* matKO embryos (Fig. 5b). This indicates that maternal PCGF1/6 deficiency leads to partial loss of H3K27me3-dependent imprinting.

Since maternal H3K27me3 also imprints *Xist*, an X-linked gene essential for X chromosome inactivation[25,26,28], we next addressed whether *Xist* is derepressed from the maternal X chromosome in *Pcgf1/6* matKO morula embryos. Simultaneous RNA/DNA fluorescence in situ hybridization (FISH) for *Xist* RNA and an X-linked DNA probe (see Methods) revealed that the majority of blastomeres in matKO female and male embryos contained two and one *Xist* RNA cloud(s), respectively (Fig. 5c and Extended Data Fig. 7c). In contrast, control female and male embryos showed one and zero cloud(s), respectively. Furthermore, analysis of RNA-seq datasets for *Pcgf1/6* matKO morula embryos demonstrated that maternal X chromosome-linked genes, but not autosomal-linked genes, are significantly downregulated (Extended Data Fig. 7d). These results indicate that *Xist* is derepressed from the maternal X chromosome, leading to aberrant maternal X chromosome inactivation in *Pcgf1/6* matKO morula embryos.

To determine whether loss of H3K27me3-dependent imprinting is caused by maternal inheritance of the H3K27me3-deficient state from FGOs, we performed H3K27me3 CUT&RUN for F_1

Fig. 4 | PCGF1/6–PRC1 deficiency causes gene-selective loss of H3K27me3 in oocytes. a,**b**, Representative images (**a**) and quantifications (**b**) of H2AK119ub1 and H3K27me3 immunostaining in *Pcgf1/6* control (CTR) and KO FGOs. Scale bar, 10 μm. The average signal intensity of the control was set to 1.0. Bars overlaid on the plots indicate means ± s.d. The numbers of FGOs examined were 36 (control) and 38 (KO). ***$P<0.001$ (two-tailed Student's *t*-test). **c**, Average signal profiles of H2AK119ub1 (the scaled sample) and H3K27me3 CUT&RUN at their broad peaks ±2 kb flanking regions in control and KO FGOs. **d**, Genome browser view of H2AK119ub1 (the scaled sample) and H3K27me3 distributions in control and KO FGOs. **e**, Heatmap showing H3K27me3 intensity in control and *Pcgf1/6* KO FGOs. Each row represents the average H3K27me3 signals within each gene body (RPKM > 1 in the control). The rightmost column indicates the relative gene expression in FGOs ($\log_2$[fold change (KO/control)]). **f**, Genome browser views of representative genes that showed loss of H3K27me3 and gene derepression in KO FGOs. **g**,**h**, MA plots of the $\log_2$[fold change (KO/control)] in gene expression in *Pcgf1/6* KO (**g**) and *Ring1a/1b* KO (**h**) FGOs. Significantly up- and downregulated genes (Benjamini–Hochberg-adjusted $P<0.01$; fold change > 2) are highlighted. The RNA-seq datasets of *Ring1a/1b* KO FGOs are from ref. [56]. **i**, Venn diagrams of up- and downregulated genes compared between *Pcgf1/6* and *Ring1a/1b* KO FGOs. The *P* values were calculated using a two-sided Fisher's exact test. **j**, Left: heatmap showing the H3K27me3 intensity in single and double KO FGOs. The order of the rows is the same as in **e**. Right: heatmap of the H3K27me3-lost and intermediate genes reordered by clustering pattern to highlight genes uniquely affected by respective single KOs. **k**, Genome browser views of representative genes that were uniquely affected by respective single KOs. Note that *Taf7l* and *Syce1* are known PCGF6–PRC1 targets.

hybrid *Pcgf1/6* control and matKO morula embryos (Extended Data Fig. 7e). Among 4,505 genes harboring maternal H3K27me3 at their gene bodies in control embryos, 361 (8.0%) showed loss of H3K27me3 in matKO embryos (fold change > 2) (Fig. 5d; group 1). Importantly, H3K27me3 had already been lost in KO FGOs at the majority of group 1 genes, which included PEGs that showed loss of imprinting at the morula stage (Fig. 5d,e and Extended Data Fig. 7f). A small population of group 1 genes, including *Xist*, showed loss of H3K27me3 at the morula stage, but not in KO FGOs (Fig. 5d,e), suggesting that H3K27me3 failed to be maintained at these genes.

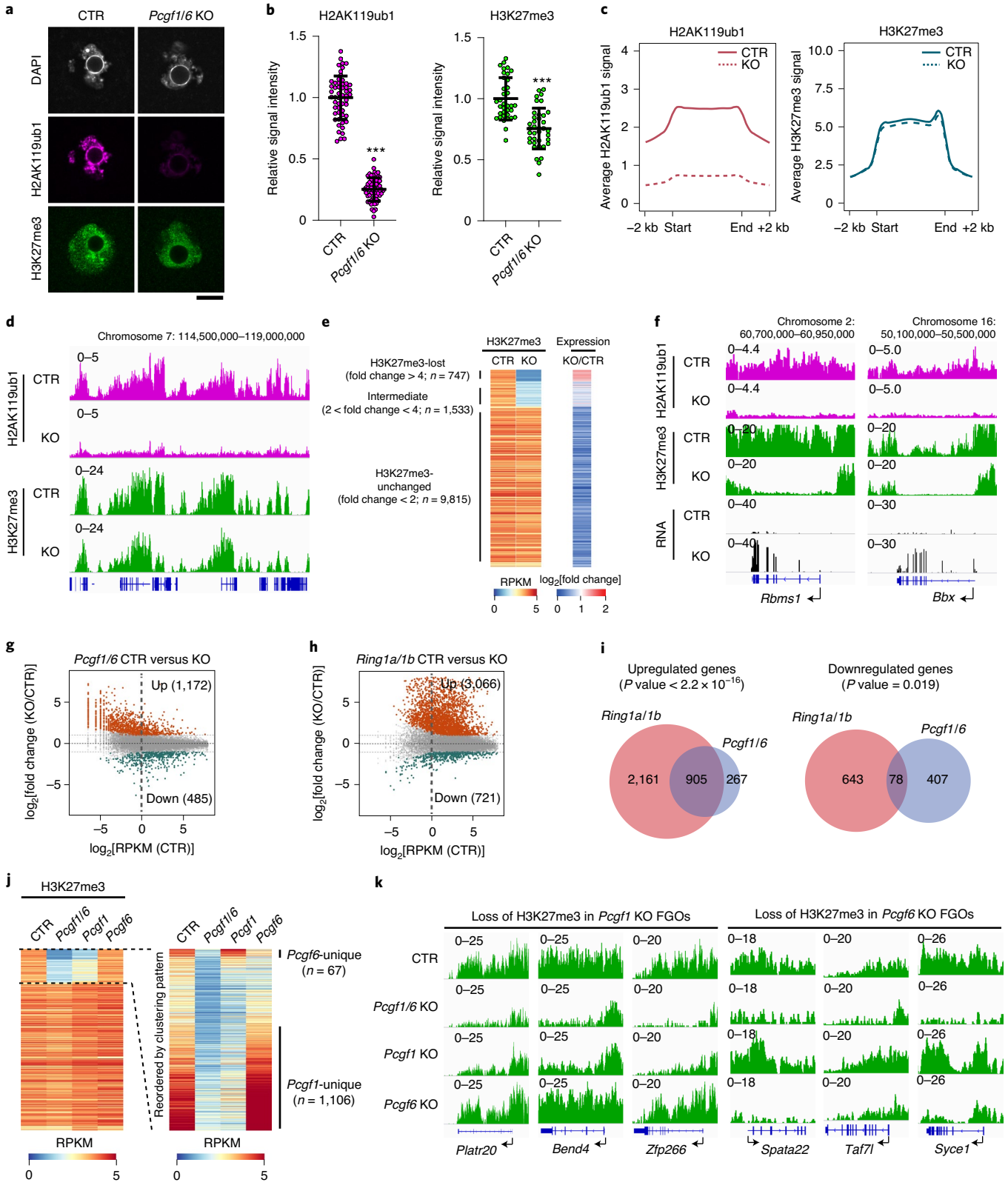

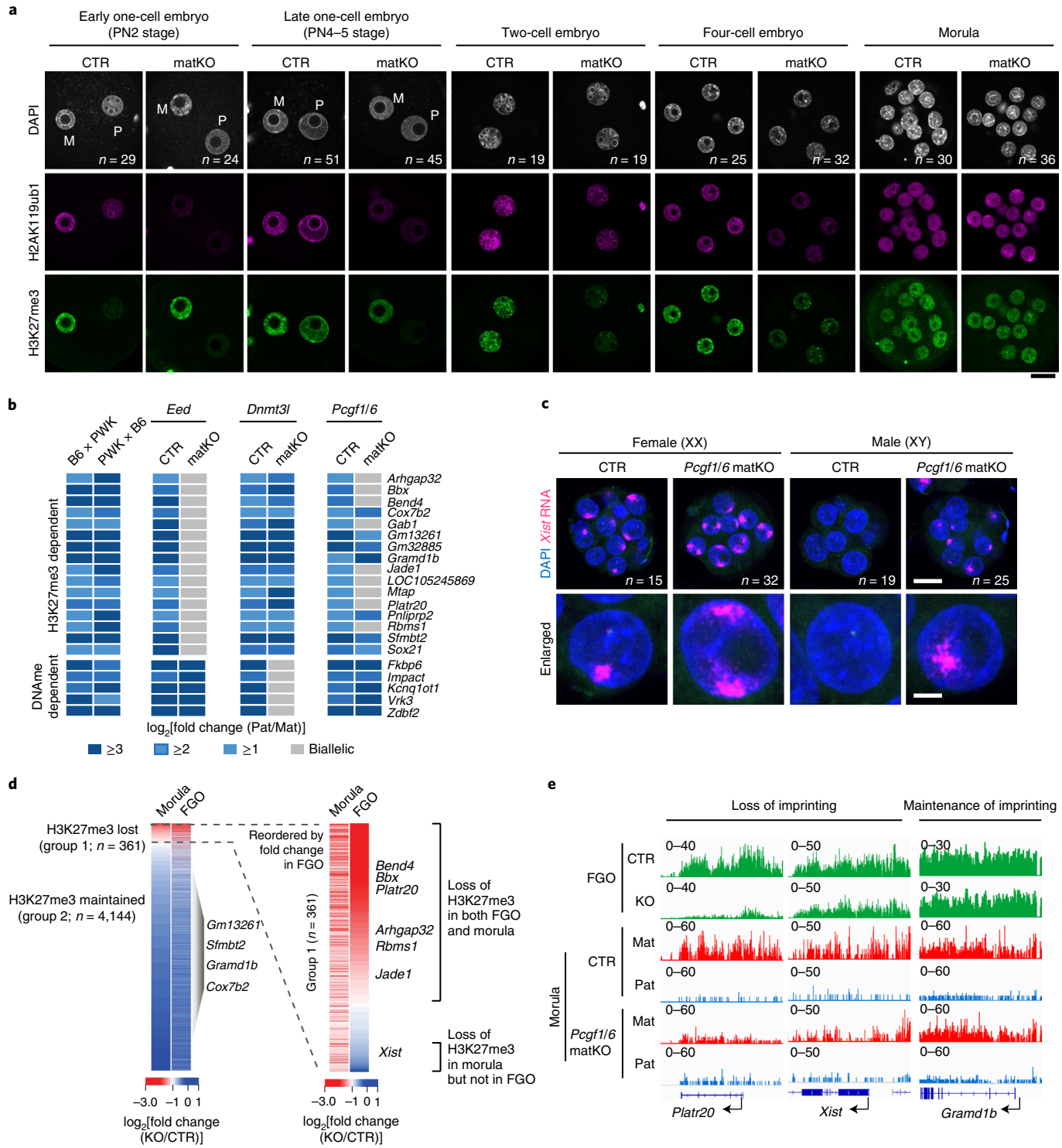

Fig. 5 | Gene-selective loss of H3K27me3 is irreversible and causes loss of H3K27me3-dependent imprinting in *Pcgf1/6* matKO embryos. a, Representative images of H2AK119ub1 and H3K27me3 immunostaining analysis in *Pcgf1/6* control and matKO embryos. M, maternal pronucleus; P, paternal pronucleus. Early (PN2) and late (PN4–5) one-cell zygotes and two-cell, four-cell and morula embryos were collected at 5, 11, 30, 46 and 72 h postfertilization, respectively. The numbers of embryos examined (*n*) are indicated. Scale bar, 20 μm. **b**, Heatmap showing the allelic expression biases of maternal H3K27me3- and DNA methylation (DNAme)-dependent PEGs in morula embryos. Genes with >20 SNP-containing reads and a fold change (Pat/Mat) > 2 in all control samples are shown. The RNA-seq datasets of *Eed* matKO and *Dnmt3l* matKO morula embryos are from ref. [26] and ref. [29], respectively. **c**, Representative images of *Xist* RNA FISH in control and matKO morula embryos. The numbers of embryos examined (*n*) are indicated. Scale bars, 20 μm (top) and 5 μm (bottom). **d**, Heatmap showing fold changes of the H3K27me3 intensity between control and matKO morula embryos and between control and KO FGOs. Each row represents a gene harboring enough H3K27me3 signals within its gene body (RPKM (mat allele) > 2 in control morula embryos)). Groups 1 and 2 represent genes that have lost H3K27me3 (fold change > 2) and maintained H3K27me3 (fold change < 2), respectively, in matKO morula embryos. The right two columns are magnified heatmaps for group 1 after reordering by the fold change values of FGOs. **e**, Genome browser views of H3K27me3 distributions in *Pcgf1/6* control and KO FGOs and control and matKO morula embryos.

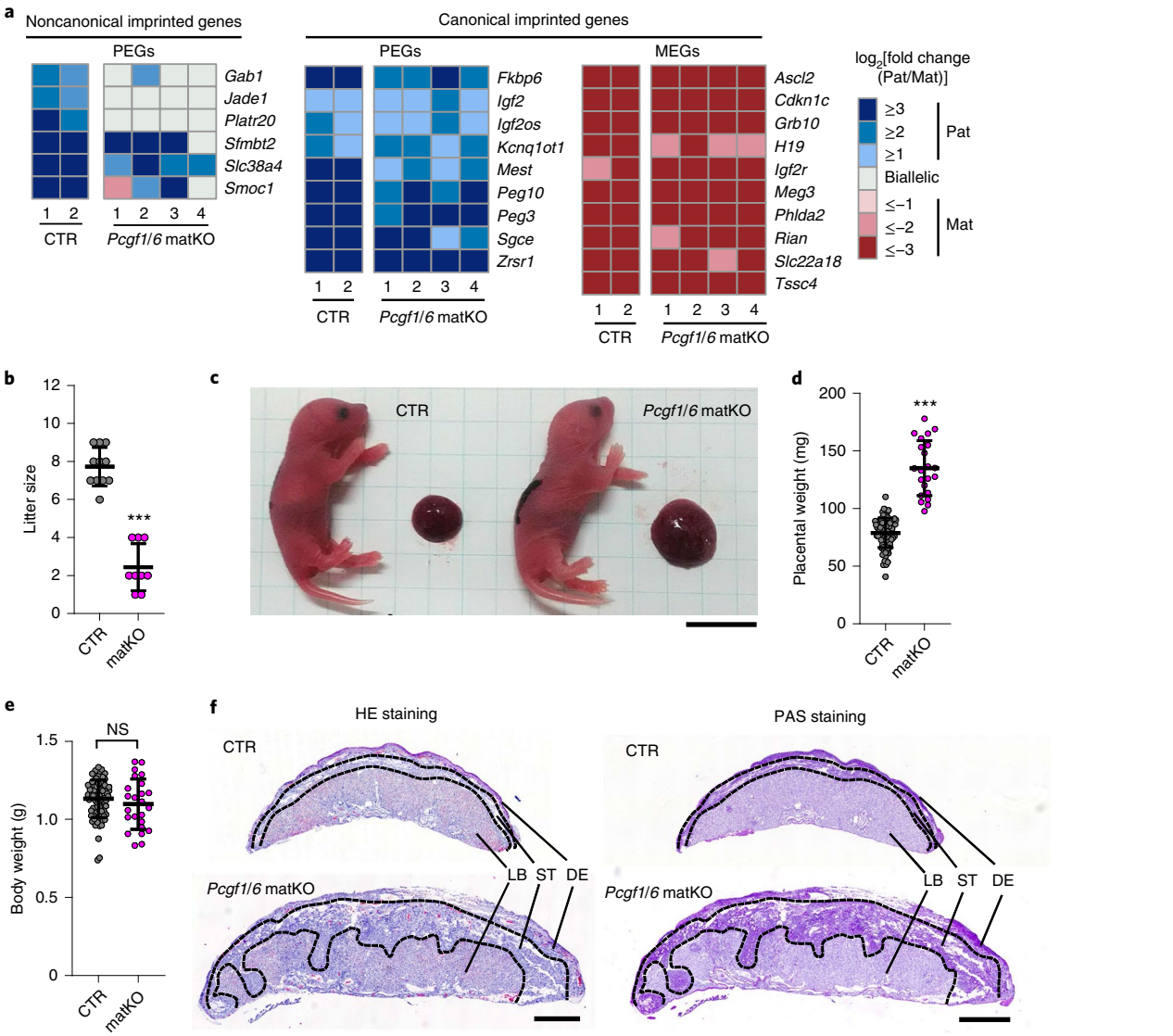

Fig. 6 | Maternal PCGF1/6–PRC1 deficiency causes placental enlargement at term. a, Heatmaps showing the allelic expression biases of maternal H3K27me3-dependent (noncanonical) imprinted genes and germline DNA-methylation-dependent (canonical) imprinted genes in extraembryonic ectoderm. MEGs, maternally expressed genes. Genes with >20 SNP-containing reads in all samples are shown. **b**, Litter sizes of *Pcgf1/6* control and matKO fetuses at E18.5. The bars overlaid on the plots indicate means ± s.d. The numbers of litters examined were 11 (control) and 10 (matKO). ***$P < 0.0001$ (two-tailed Student's *t*-test). **c**, Representative images of fetuses and placentae at E18.5. Scale bar, 10 mm. **d**,**e**, Placental weights (**d**) and body weights (**e**) of *Pcgf1/6* control and matKO fetuses at E18.5. The bars overlaid on the plots indicate means ± s.d. The numbers of placentae were 85 (control) and 24 (matKO). ***$P < 0.0001$ (two-tailed Student's *t*-test). NS, not significant. **f**, Representative images of placental sections stained with hematoxylin and eosin (HE) and periodic acid Schiff (PAS) staining. DE, maternal decidua; LB, labyrinthine layer; ST, spongiotrophoblast layer. Scale bars, 1 mm. The numbers of placentae examined were 5 (control) and 7 (matKO).

Group 2 genes retained H3K27me3 in matKO embryos, which included PEGs that maintained imprinted expression (Fig. 5d,e and Extended Data Fig. 7f). Consistent with the immunofluorescence analysis, quantitative H3K27me3 CUT&RUN analysis at the late two-cell stage confirmed that H3K27me3 levels in matKO embryos are globally lower than those in control embryos (Extended Data Fig. 7g,h), which may contribute to failure in H3K27me3 maintenance at some group 1 genes, such as *Xist*. It was also notable that maternal H3K27me3 at group 2 genes is not completely lost in matKO two-cell embryos (Extended Data Fig. 7i), suggesting that residual H3K27me3 seeds for its recovery by the morula stage. These H3K27me3-associated genes keep associating with H2AK119ub1 in wild-type preimplantation embryos (Extended Data Fig. 7i), further pointing to a possible contribution of H2AK119ub1 to H3K27me3 homeostasis. Hence, we conclude that, despite fluctuation of global H3K27me3 levels, the gene-selective deficient state of H3K27me3 is irreversibly inherited by embryos, which causes loss of H3K27me3-dependent imprinting in *Pcgf1/6* matKO embryos.

Defective noncanonical imprinting and placental enlargement. To determine whether maternal PCGF1/6 deficiency impacts postimplantation development, we first dissected *Pcgf1/6* matKO embryos at embryonic day 6.5 (E6.5). The average number of implantations in matKO embryos (3.8 ± 2.3) was lower than that in control embryos (8.8 ± 0.5) (Extended Data Fig. 8a), presumably due to the impaired preimplantation development. All of the matKO embryos were remarkably smaller than control embryos, despite restoration of the aberrant X chromosome inactivation

(Extended Data Fig. 8b,c), which recapitulated *Eed* matKO embryos that lacked maternal H3K27me3-dependent imprinting[26]. Given that a few H3K27me3-dependent PEGs maintain their allelic expression in extraembryonic cells (termed noncanonical imprinting)[26,27,29,30], we performed allelic RNA-seq analysis of extraembryonic ectoderm, which gives rise to placental tissues (Extended Data Fig. 8d,e and Supplementary Table 6). The paternal expression biases of six noncanonical imprinted genes were lost or became milder in *Pcgf1/6* matKO embryos, with some interembryonic variation in genes such as *Sfmbt2* and *Smoc1* (Fig. 6a). None of the DNA-methylation-dependent (canonical) imprinted genes lost imprinting in matKO embryos (Fig. 6a). These results demonstrate that *Pcgf1/6* matKO embryos continuously show defective noncanonical imprinting in extraembryonic cells.

Next, we performed cesarean section (C-section) at E18.5 and found that 2.4 ± 1.2 *Pcgf1/6* matKO and 7.7 ± 1.0 control fetuses reached term (Fig. 6b and Extended Data Fig. 9a). The fetus/implantation ratio of matKO fetuses (24/44; 55%) was lower than that of control fetuses (85/89; 96%) (Extended Data Fig. 9a), indicating a higher incidence of postimplantation death due to yet-to-be-determined reasons in the matKO. Remarkably, matKO placentae were 73% heavier than those of control ones, while their body weights were comparable (Fig. 6c–e). Histological analysis showed expansion of the spongiotrophoblast layer and invasion of glycogen-positive spongiotrophoblast cells into the labyrinth layer (Fig. 6f). This abnormality was indicative of overproliferation of fetus-derived cells[66]. The placental enlargement of matKO was not due to the smaller litter size, because it was reproduced by transplantation of matKO embryos together with control embryos into a single surrogate mother (Extended Data Fig. 9b–d). Furthermore, C-section of wild-type females mated with *Pcgf1/6* double heterozygous males confirmed that the sublethality and placental enlargement are not caused by haploinsufficiency of *Pcgf1/6* (Extended Data Fig. 9e,f). Moreover, C-section of *Pcgf1* and *Pcgf6* single matKO mice showed no developmental lethality and a very modest increase of the placental weight (Extended Data Fig. 9g–j). These results demonstrate that maternal PRC1.1 and PRC1.6 synergistically function for maternal epigenetic inheritance that ensures proper embryonic and placental development.

Discussion

Temporal in vivo dynamics of H2AK119ub1 and H3K27me3 revealed that H2AK119ub1 is progressively deposited after the one-cell stage, whereas H3K27me3 emerges from or after the blastocyst stage. Since many typical PcG target genes follow this order, H2AK119ub1 potentially primes zygotic Polycomb domain formation. The H2AK119ub1–H3K27me3 hierarchical pathway has previously been appreciated in experimentally manipulated contexts, such as genetic perturbations and synthetic de novo targeting assays[40,42–49]. Importantly, our study captures stepwise deposition of H2AK119ub1 followed by H3K27me3 in a physiological context. The temporal gap between the deposition of H2AK119ub1 and H3K27me3 creates a unique epigenetic state in preimplantation embryos where H2AK119ub1 alone exists at the developmentally relevant genes, which might confer cell fate plasticity to these embryos. Mechanistically, the function of PRC2.2, which can deposit H3K27me3 downstream of H2AK119ub1 (ref. [37]), might be repressed in preimplantation embryos. Future studies should reveal the mechanism and importance of the successive deposition of H2AK119ub1 and H3K27me3 during early development.

Mouse oocytes form unique histone PTM landscapes when they arrest the cell cycle during oocyte growth, which allows the study of cell cycle-independent mechanisms of epigenetic regulation. Here, we found that H2AK119ub1 was massively reduced, but only a subset of genes lost H3K27me3, in *Pcgf1/6* KO oocytes. This is in sharp contrast with vPRC1 KO mESCs, in which both H2AK119ub1 and H3K27me3 are globally lost[41]. We speculate that vPRC1-mediated H2AK119ub1 may be a prerequisite for H3K27me3 maintenance in dividing cells. In support of this notion, we observed that H3K27me3 is globally reduced in *Pcgf1/6* matKO zygotes upon their entry into mitotic cell cycles, and that loss of H2AK119ub1 precedes that of H3K27me3 at gene deserts during preimplantation development. Thus, our study highlights potential differences in the mode of Polycomb system function between dividing and nondividing cells in which H3K27me3 homeostasis is, respectively, more and less dependent on H2AK119ub1.

There are two nonexclusive scenarios for how H2AK119ub1 reduction leads to H3K27me3 loss and gene derepression in *Pcgf1/6* KO oocytes. First, H2AK119ub1 reduction could result in PRC2.2 dissociation, which in turn causes H3K27me3 loss and gene derepression. This scenario is partly supported by a recent study showing that acute PRC1-depletion-induced loss of H2AK119ub1 causes rapid dissociation of PRC2 before gene derepression in mESCs[67]. Second, H2AK119ub1 reduction results in gene derepression, which in turn causes PRC2 dissociation and H3K27me3 loss. This scenario is in line with the observations that active transcription causes exclusion of H3K27me3 from gene bodies during oocyte growth[18], as well as PRC2 dissociation in mESCs[68]. It is also supported by the high correlation between H3K27me3 loss and gene derepression in *Pcgf1/6* KO FGOs. If the second scenario is the case, it is theoretically possible that H2AK119ub1 and H3K27me3 are independently and promiscuously deposited at nontranscribing regions in oocytes. Further investigations are warranted to clarify these points.

Gene-selective loss of H3K27me3 allowed us to gain important insights into intergenerational epigenetic inheritance. Previously, we and others have generated *Eed* KO oocytes, which lost H3K27me3 genome wide, to study the functions of maternally inherited H3K27me3 (refs. [25,26]). However, because PRC2 is continuously inactive until around the eight-cell stage, the *Eed* matKO model failed to show whether the H3K27me3-deficient state can be inherited even in the presence of active PRC2. Characterization of *Pcgf1/6* matKO embryos revealed that this is indeed the case, as the selective loss state was irreversible in the embryos. This notion was further supported by a recent observation that aberrant H3K27me3 distribution in *Setd2* KO oocytes persists after fertilization[15]. Importantly, we demonstrated that maternal inheritance of H3K27me3-deficient states causes long-term consequences in postimplantation development and placentae. These studies raise the intriguing possibility that changes in histonePTMs of ovarian oocytes, which might be induced by the maternal environment, can no longer be repaired once they are transmitted to embryos.

Recent knowledge of Polycomb-mediated gene silencing mechanisms led us to reconsider the molecular basis of maternal H3K27me3-dependent imprinting. In preimplantation embryos, the maternal allele silencing is apparently dependent on H3K27me3, because H3K27me3, but not H2AK119ub1, maintains maternal allele-specific distribution, and *Eed* KO or *Kdm6b* overexpression induces maternal allele derepression[25–28]. However, in FGOs, H3K27me3-associated genes remain silenced upon *Eed* KO, while they are derepressed in *Ring1a/1b* KO[56]. Concurrently, Polycomb-associating domains are disrupted in *Ring1a/1b*, but not *Eed*, KO FGOs[56]. Interestingly, Polycomb-associating domains are attenuated after the two-cell stage and lost by the blastocyst stage[9,56], while maternal H3K27me3 is maintained. These findings suggest that maternal Polycomb-dependent imprinting is established by PRC1-mediated H2AK119ub1 during oogenesis and then maintained by more static H3K27me3 during preimplantation development, probably via self-sustaining activity of PRC2 (ref. [69]).

The placenta is an essential extraembryonic organ that provides an interface for gas and nutrient exchange between the mother and fetus. We found that maternal deficiency of PCGF1/6 causes loss of noncanonical imprinting in the extraembryonic cells, leading

to placental enlargement. Curiously, placental enlargement is also observed in cloned mice in which noncanonical imprinted genes are biallelically expressed[66,70,71], and it is ameliorated by restoration of the monoallelic expression in cloned mice[72,73]. This suggests that loss of noncanonical imprinting could be the cause of placental enlargement in *Pcgf1/6* matKO mice. Further studies are needed to understand how noncanonical imprinting regulates placental development. Additionally, it is fascinating that noncanonical imprinting also follows the parental conflict theory, in which loss of maternal imprints is expected to enhance the growth of fetuses and/or placentae[74]. This also brings to mind a matKO mutant of *MEDEA*, a mammalian *Ezh1/2* ortholog in *Arabidopsis thaliana* that exhibits overproliferation of endosperm-derived cells[75]. Our study thus sheds light on the conserved function of maternal Polycomb systems in the regulation of extraembryonic tissue size in both mammals and plants.

Online content

Any methods, additional references, Nature Research reporting summaries, source data, extended data, supplementary information, acknowledgements, peer review information; details of author contributions and competing interests; and statements of data and code availability are available at https://doi.org/10.1038/s41588-021-00820-3.

Received: 11 September 2020; Accepted: 17 February 2021;
Published online: 5 April 2021

References

1. Eckersley-Maslin, M. A., Alda-Catalinas, C. & Reik, W.Dynamics of the epigenetic landscape during the maternal-to-zygotic transition. *Nat. Rev. Mol. Cell Biol.* **19**, 436–450 (2018).
2. Borsos, M. et al. Genome–lamina interactions are established de novo in the early mouse embryo. *Nature* **569**, 729–733 (2019).
3. Burton, A. & Torres-Padilla, M. Epigenetic reprogramming and development: a unique heterochromatin organization in the preimplantation mouse embryo. *Brief. Funct. Genomics* **9**, 444–454 (2010).
4. Burton, A. & Torres-Padilla, M. Chromatin dynamics in the regulation of cell fate allocation during early embryogenesis. *Nat. Rev. Mol. Cell Biol.* **15**, 723–735 (2014).
5. Xu, Q. & Xie, W. Epigenome in early mammalian development: inheritance, reprogramming and establishment. *Trends Cell Biol.* **28**, 237–253 (2018).
6. Probst, A. & Almouzni, G. Heterochromatin establishment in the context of genome-wide epigenetic reprogramming. *Trends Genet.* **27**, 177–185 (2011).
7. Duffie, R. & Bourc'his, D. Parental epigenetic asymmetry in mammals. *Curr. Top. Dev. Biol.* **104**, 293–328 (2013).
8. Feil, R. Epigenetic asymmetry in the zygote and mammalian development. *Int. J. Dev. Biol.* **53**, 191–201 (2009).
9. Collombet, S. et al. Parental-to-embryo switch of chromosome organization in early embryogenesis. *Nature* **580**, 142–146 (2020).
10. Flyamer, I. M. et al. Single-nucleus Hi-C reveals unique chromatin reorganization at oocyte-to-zygote transition. *Nat. Genet.* **544**, 110–114 (2017).
11. Du, Z. et al. Allelic reprogramming of 3D chromatin architecture during early mammalian development. *Nature* **547**, 232–235 (2017).
12. Ke, Y. et al. 3D chromatin structures of mature gametes and structural reprogramming during mammalian embryogenesis. *Cell* **170**, 367–381.e20 (2017).
13. Liu, X. et al. Distinct features of H3K4me3 and H3K27me3 chromatin domains in pre-implantation embryos. *Nature* **537**, 558–562 (2016).
14. Wang, C. et al. Reprogramming of H3K9me3-dependent heterochromatin during mammalian embryo development. *Nat. Cell Biol.* **20**, 620–631 (2018).
15. Xu, Q. et al. SETD2 regulates the maternal epigenome, genomic imprinting and embryonic development. *Nat. Genet.* **51**, 844–856 (2019).
16. Zhang, B. et al. Allelic reprogramming of the histone modification H3K4me3 in early mammalian development. *Nature* **537**, 553–557 (2016).
17. Dahl, J. A. et al. Broad histone H3K4me3 domains in mouse oocytes modulate maternal-to-zygotic transition. *Nature* **537**, 548–552 (2016).
18. Zheng, H. et al. Resetting epigenetic memory by reprogramming of histone modifications in mammals. *Mol. Cell* **63**, 1066–1079 (2016).
19. Hanna, C. W. et al. MLL2 conveys transcription-independent H3K4 trimethylation in oocytes. *Nat. Struct. Mol. Biol.* **25**, 73–82 (2018).
20. Sankar, A. et al. KDM4A regulates the maternal-to-zygotic transition by protecting broad H3K4me3 domains from H3K9me3 invasion in oocytes. *Nat. Cell Biol.* **22**, 380–388 (2020).
21. Yeung, W. K. A. et al. Histone H3K9 methyltransferase G9a in oocytes is essential for preimplantation development but dispensable for CG methylation protection. *Cell Rep.* **27**, 282–293.e4 (2019).
22. Tucci, V. et al. Genomic imprinting and physiological processes in mammals. *Cell* **176**, 952–965 (2019).
23. Ferguson-Smith, A. C. Genomic imprinting: the emergence of an epigenetic paradigm. *Nat. Rev. Genet.* **12**, 565–575 (2011).
24. Chen, Z. & Zhang, Y. Maternal H3K27me3-dependent autosomal and X chromosome imprinting. *Nat. Rev. Genet.* **21**, 555–571 (2020).
25. Harris, C. et al. Conversion of random X-inactivation to imprinted X-inactivation by maternal PRC2. *eLife* **8**, e44258 (2019).
26. Inoue, A., Chen, Z., Yin, Q. & Zhang, Y. Maternal *Eed* knockout causes loss of H3K27me3 imprinting and random X inactivation in the extraembryonic cells. *Genes Dev.* **32**, 1525–1536 (2018).
27. Inoue, A., Jiang, L., Lu, F., Suzuki, T. & Zhang, Y. Maternal H3K27me3 controls DNA methylation-independent imprinting. *Nature* **547**, 419–424 (2017).
28. Inoue, A., Jiang, L., Lu, F. & Zhang, Y. Genomic imprinting of *Xist* by maternal H3K27me3. *Genes Dev.* **31**, 1927–1932 (2017).
29. Chen, Z., Inoue, A., Yin, Q., Zhang, C. & Zhang, Y. Allelic H3K27me3 to allelic DNA methylation switch maintains noncanonical imprinting in extraembryonic cells. *Sci. Adv.* **5**, eaay7246 (2019).
30. Hanna, C. W. et al. Endogenous retroviral insertions drive non-canonical imprinting in extra-embryonic tissues. *Genome Biol.* **20**, 225 (2019).
31. Gaydos, L. J., Wang, W. & Strome, S. Gene repression. H3K27me and PRC2 transmit a memory of repression across generations and during development. *Science* **345**, 1515–1518 (2014).
32. Batista, R. A. & Köhler, C. Genomic imprinting in plants—revisiting existing models. *Genes Dev.* **34**, 24–36 (2020).
33. Zenk, F. et al. Germ line-inherited H3K27me3 restricts enhancer function during maternal-to-zygotic transition. *Science* **357**, 212–216 (2017).
34. Skvortsova, K., Iovino, N. & Bogdanovic, O. Functions and mechanisms of epigenetic inheritance in animals. *Nat. Rev. Mol. Cell Biol.* **19**, 774–790 (2018).
35. Schuettengruber, B., Bourbon, H.-M., Di Croce, L. & Cavalli, G. Genome regulation by Polycomb and Trithorax: 70 years and counting. *Cell* **171**, 34–57 (2017).
36. Aranda, S., Mas, G. & Di Croce, L. Regulation of gene transcription by Polycomb proteins. *Sci. Adv.* **1**, e1500737 (2015).
37. Blackledge, N. P., Rose, N. R. & Klose, R. J. Targeting Polycomb systems to regulate gene expression: modifications to a complex story. *Nat. Rev. Mol. Cell Biol.* **16**, 643–649 (2015).
38. Barbour, H., Daou, S., Hendzel, M. & Affar, E. B. Polycomb group-mediated histone H2A monoubiquitination in epigenome regulation and nuclear processes. *Nat. Commun.* **11**, 5947 (2020).
39. Gao, Z. et al. PCGF homologs, CBX proteins, and RYBP define functionally distinct PRC1 family complexes. *Mol. Cell* **45**, 344–356 (2012).
40. Blackledge, N. P. et al. Variant PRC1 complex-dependent H2A ubiquitylation drives PRC2 recruitment and Polycomb domain formation. *Cell* **157**, 1445–1459 (2014).
41. Fursova, N. A. et al. Synergy between variant PRC1 complexes defines Polycomb-mediated gene repression. *Mol. Cell* **74**, 1020–1036.e8 (2019).
42. Blackledge, N. P. et al. PRC1 catalytic activity is central to Polycomb system function. *Mol. Cell* **77**, 857–874.e9 (2020).
43. Tamburri, S. et al. Histone H2AK119 mono-ubiquitination is essential for Polycomb-mediated transcriptional repression. *Mol. Cell* **77**, 840–856.e5 (2020).
44. Tavares, L. et al. RYBP–PRC1 complexes mediate H2A ubiquitylation at Polycomb target sites independently of PRC2 and H3K27me3. *Cell* **148**, 664–678 (2012).
45. Almeida, M. et al. PCGF3/5–PRC1 initiates Polycomb recruitment in X chromosome inactivation. *Science* **356**, 1081–1084 (2017).
46. Cooper, S. et al. Targeting Polycomb to pericentric heterochromatin in embryonic stem cells reveals a role for H2AK119u1 in PRC2 recruitment. *Cell Rep.* **7**, 1456–1470 (2014).
47. Cooper, S. et al. Jarid2 binds mono-ubiquitylated H2A lysine 119 to mediate crosstalk between Polycomb complexes PRC1 and PRC2. *Nat. Commun.* **7**, 13661 (2016).
48. Kalb, R. et al. Histone H2A monoubiquitination promotes histone H3 methylation in Polycomb repression. *Nat. Struct. Mol. Biol.* **21**, 569–571 (2014).
49. Rose, N. R. et al. RYBP stimulates PRC1 to shape chromatin-based communication between Polycomb repressive complexes. *eLife* **5**, e18591 (2016).

50. Pintacuda, G. et al. hnRNPK recruits PCGF3/5–PRC1 to the Xist RNA B-repeat to establish Polycomb-mediated chromosomal silencing. *Mol. Cell* **68**, 955–969.e10 (2017).
51. Skene, P. J. & Henikoff, S. An efficient targeted nuclease strategy for high-resolution mapping of DNA binding sites. *eLife* **6**, e21856 (2017).
52. Scelfo, A. et al. Functional landscape of PCGF proteins reveals both RING1A/B-dependent-and RING1A/B-independent-specific activities. *Mol. Cell* **74**, 1037–1052.e7 (2019).
53. Van den Boom, V. et al. Non-canonical PRC1.1 targets active genes independent of H3K27me3 and Is essential for leukemogenesis. *Cell Rep.* **14**, 332–346 (2016).
54. Zhou, Y., Romero-Campero, F. J., Gomez-Zambrano, A., Turck, F. & Calonje, M. H2A monoubiquitination in *Arabidopsis thaliana* is generally independent of LHP1 and PRC2 activity. *Genome Biol.* **18**, 69 (2017).
55. Loubiere, V., Papadopoulos, G. L., Szabo, Q., Martinez, A.-M. & Cavalli, G. Widespread activation of developmental gene expression characterized by PRC1-dependent chromatin looping. *Sci. Adv.* **6**, eaax4001 (2020).
56. Du, Z. et al. Polycomb group proteins regulate chromatin architecture in mouse oocytes and early embryos. *Mol. Cell* **77**, 825–839.e7 (2020).
57. Posfai, E. et al. Polycomb function during oogenesis is required for mouse embryonic development. *Genes Dev.* **26**, 920–932 (2012).
58. Puschendorf, M. et al. PRC1 and Suv39h specify parental asymmetry at constitutive heterochromatin in early mouse embryos. *Nat. Genet.* **40**, 411–420 (2008).
59. Tardat, M. et al. Cbx2 targets PRC1 to constitutive heterochromatin in mouse zygotes in a parent-of-origin-dependent manner. *Mol. Cell* **58**, 157–171 (2015).
60. Eid, A. & Torres-Padilla, M. E. Characterization of non-canonical Polycomb repressive complex 1 subunits during early mouse embryogenesis. *Epigenetics* **11**, 389–397 (2016).
61. De Vries, W. N. et al. Expression of Cre recombinase in mouse oocytes: a means to study maternal effect genes. *Genesis* **26**, 110–112 (2000).
62. Zepeda-Martinez, J. A. et al. Parallel PRC2/cPRC1 and vPRC1 pathways silence lineage-specific genes and maintain self-renewal in mouse embryonic stem cells. *Sci. Adv.* **6**, eaax5692 (2020).
63. Endoh, M. et al. PCGF6–PRC1 suppresses premature differentiation of mouse embryonic stem cells by regulating germ cell-related genes. *eLife* **6**, e21064 (2017).
64. Stielow, B., Finkernagel, F., Stiewe, T., Nist, A. & Suske, G. MGA, L3MBTL2 and E2F6 determine genomic binding of the non-canonical Polycomb repressive complex PRC1.6. *PLoS Genet.* **14**, e1007193 (2018).
65. Farcas, A. M. et al. KDM2B links the Polycomb repressive complex 1 (PRC1) to recognition of CpG islands. *eLife* **1**, e00205 (2012).
66. Matoba, S. et al. Loss of H3K27me3 imprinting in somatic cell nuclear transfer embryos disrupts post-implantation development. *Cell Stem Cell* **23**, 343–354.e5 (2018).
67. Dobrinić, P., Szczurek, A. T. & Klose, R. J. PRC1 drives Polycomb-mediated gene repression by controlling transcription initiation and burst frequency. Preprint at *bioRxiv* https://doi.org/10.1101/2020.10.09.333294 (2020).
68. Riising, E. M. et al. Gene silencing triggers Polycomb repressive complex 2 recruitment to CpG islands genome wide. *Mol. Cell* **55**, 347–360 (2014).
69. Yu, J.-R., Lee, C.-H., Oksuz, O., Stafford, J. M. & Reinberg, D. PRC2 is high maintenance. *Genes Dev.* **33**, 903–935 (2019).
70. Wakayama, T. & Yanagimachi, R.Cloning of male mice from adult tail-tip cells. *Nat. Genet.* **22**, 127–128 (1999).
71. Okae, H. et al. RNA sequencing-based identification of aberrant imprinting in cloned mice. *Hum. Mol. Genet.* **23**, 992–1001 (2014).
72. Wang, L. Y. et al. Overcoming intrinsic H3K27me3 imprinting barriers improves post-implantation development after somatic cell nuclear transfer. *Cell Stem Cell* **27**, 315–325.e5 (2020).
73. Inoue, K. et al. Loss of H3K27me3 imprinting in the Sfmbt2 miRNA cluster causes enlargement of cloned mouse placentas. *Nat. Commun.* **11**, 2150 (2020).
74. Haig, D. Parental antagonism, relatedness asymmetries, and genomic imprinting. *Proc. Biol. Sci.* **264**, 1657–1662 (1997).
75. Grossniklaus, U., Vielle-Calzada, J. P., Hoeppner, M. A. & Gagliano, W. B. Maternal control of embryogenesis by MEDEA, a Polycomb group gene in *Arabidopsis*. *Science* **280**, 446–450 (1998).
76. Healy, E. et al. PRC2.1 and PRC2.2 synergize to coordinate H3K27 trimethylation. *Mol. Cell* **76**, 437–452.e6 (2019).

Methods

Animal care. All of the animal experiments were performed in accordance with the guidelines of the Institutional Animal Care and Use Committee at RIKEN Center for Integrative Medical Sciences. Same-sex littermates were housed in groups of up to five mice per ventilated cage with nesting materials. The mouse facility was kept at 21–25 °C and 40–60% humidity with a 12-h light/12-h dark cycle.

Collection of mouse oocytes. All of the animal experiments were performed in accordance with the guidelines of the Institutional Animal Care and Use Committee at RIKEN Center for Integrative Medical Sciences. Fully grown germinal vesicle-stage oocytes (FGOs) were obtained from 4-week-old C57BL/6NCrl (B6N) females (Oriental Yeast) 44–48 h after injection with 0.15 ml CARD HyperOva (Kyudo). The ovaries were transferred to HEPES-buffered KSOM containing 0.2 mM 3-isobutyl-1-methylxanthine (IBMX; Merck). The ovarian follicles were punctured with a 27-gauge needle and the cumulus cells were gently removed from the cumulus–oocyte complexes (COCs) using a narrow-bore glass pipette. FGOs were then transferred into KSOM containing 0.2 mM IBMX. Growing oocytes were collected from 7-d-old B6N females. The ovaries were transferred to HEPES–KSOM containing 1 mg ml^{-1} collagenase (Merck; C9263-100MG) and incubated for 2–3 h at 37 °C with gentle pipetting every 30 min. Denuded growing oocytes were then harvested using a glass pipette. For CUT&RUN sample collection, FGOs and growing oocytes were briefly incubated in acidic Tyrode's solution (Merck Millipore; MR-004-D) to remove the zona pellucida, then washed in HEPES–KSOM, followed by 0.2% bovine serum albumin (BSA)/phosphate-buffered saline (PBS). Approximately 500 oocytes were collected for each CUT&RUN experiment.

Collection of mouse preimplantation embryos. For superovulation, 4- to 10-week-old B6N females were injected with 7.5 IU pregnant mare serum gonadotropin (ASKA Pharmaceutical) or 0.15 ml CARD HyperOva followed by 7.5 IU human chorionic gonadotropin (ASKA Pharmaceutical) at a 48-h interval. When collecting MII oocytes for CUT&RUN, COCs were harvested 15–17 h after human chorionic gonadotropin injection and incubated in M2 media containing hyaluronidase (Merck Millipore; MR-051-F) to remove cumulus cells. For in vitro fertilization, COCs were inseminated with activated spermatozoa in Human Tubal Fluid medium supplemented with 10 mg ml^{-1} BSA (Merck Millipore; 12657). Spermatozoa were obtained from the caudal epididymis of adult PWK/PhJ mice (RBRC00213 (RIKEN BioResource Research Center) originated from 003715 (The Jackson Laboratory)) and B6D2F1 (Oriental Yeast) male mice. Spermatozoa were capacitated by 1 h incubation in CARD FERTIUP (Kyudo) for PWK sperm or in Human Tubal Fluid medium for BDF1 sperm. When generating PWK/B6 F_1 hybrid embryos, COCs were collected from superovulated 4-month-old PWK females and inseminated with activated spermatozoa that were obtained from adult B6N males. At 6–8 h postinsemination, zygotes with two pronuclei were transferred to KSOM (Merck Millipore; MR-020P-D) and cultured under a humidified atmosphere with 5% CO_2/95% air at 37.8 °C. For CUT&RUN sample collection, MII oocytes, zygotes and preimplantation embryos were briefly incubated in acidic Tyrode's solution supplemented with 0.5% polyvinylpyrrolidone and 50 mM NaCl to gently remove the zona pellucida, then washed in M2 media (Merck Millipore; MR-015-D). Polar bodies of zygotes were removed by gentle pipetting with a narrow glass capillary in M2 media containing 5 µg ml^{-1} cytochalasin B (Merck; C6762) and 0.1 µg ml^{-1} colcemid (Merck; 10295892001). Polar bodies of two-cell embryos were removed by gentle pipetting in trypsin/EDTA solution (Merck; T4049) supplemented with 0.5% polyvinylpyrrolidone. After polar body removal, zygotes/embryos were washed with M2 media followed by 0.2% BSA/PBS. PN5 zygotes, as well as early two-cell, late two-cell, morula and blastocyst embryos, were collected at 11–12, 18–19, 30, 72 and 96 h postinsemination with 500–1,000 blastomeres collected for each CUT&RUN experiment.

CUT&RUN. CUT&RUN libraries were prepared as previously described[26]. For quantitative CUT&RUN, a certain number of *Drosophila melanogaster* S2 cells (Thermo Fisher Scientific; R69007) were first captured using BioMag Plus Concanavalin A beads (Bangs Laboratories). After the beads were thoroughly resuspended, they were split into two 1.5-ml tubes, then an equal number of control and KO FGOs or embryos were added to each of the tubes. For quantitative H2AK119ub1 CUT&RUN in 500 control and KO FGOs, 800 S2 cells per sample were used. For quantitative H3K27me3 CUT&RUN in 80 late two-cell control and matKO embryos, 300 S2 cells per sample were used. The antibodies used were rabbit anti-H2AK119ub1 (1/100; Cell Signaling Technology; 8240) and rabbit anti-H3K27me3 antibody (1/100; Diagenode; C15410069). The specificity of the H3K27me3 antibody for CUT&RUN was proven in a previous study[26]. Protein A-MNase was provided by S. Henikoff's laboratory[51]. CUT&RUN libraries were sequenced on a NextSeq 500 with paired- or single-end 75-base pair (bp) reads (Illumina).

Generation of oocyte-specific *Pcgf1/6* conditional KO mice. The *Pcgf1*^{flox} mouse line was established previously[45]. The *Pcgf6*^{flox} mouse line was generated from a *Pcgf6*^{flox} ESC line that was described previously[63]. The ESCs were aggregated with eight-cell-stage embryos to generate chimeric mice that were then mated with B6;SJL-Tg(ACTFLPe)9025Dym/J mice (The Jackson Laboratory; 003800) to remove the neomycin resistance gene cassette. Both mouse lines are on a B6/129 mixed background. The *Pcgf1*^{flox} and *Pcgf6*^{flox} females were crossed with a *Zp3*^{Cre} mouse line (The Jackson Laboratory; C57BL/6-Tg(Zp3-cre)93Knw/J; 003651) to obtain *Zp3*^{Cre}/*Pcgf1*$^{flox/flox}$/*Pcgf6*$^{flox/flox}$ males and *Pcgf1*$^{flox/flox}$/*Pcgf6*$^{flox/flox}$ females. These were intercrossed to obtain *Pcgf1*$^{flox/flox}$/*Pcgf6*$^{flox/flox}$ (control) and *Zp3*^{Cre}/*Pcgf1*$^{flox/flox}$/*Pcgf6*$^{flox/flox}$ (conditional double KO) females for our experiments. The respective single KO females (that is, *Zp3*^{Cre}/*Pcgf1*$^{flox/flox}$/*Pcgf6*$^{+/+}$ or *Zp3*^{Cre}/*Pcgf1*$^{flox/flox}$/*Pcgf6*$^{+/flox}$ (*Pcgf1* conditional single KO) and *Zp3*^{Cre}/*Pcgf1*$^{+/+}$/*Pcgf6*$^{flox/flox}$ or *Zp3*^{Cre}/*Pcgf1*$^{+/flox}$/*Pcgf6*$^{flox/flox}$ (*Pcgf6* conditional single KO)) were obtained by backcrossing the *Zp3*^{Cre}/*Pcgf1*$^{flox/flox}$/*Pcgf6*$^{flox/flox}$ males with B6N followed by intercrossing. Double heterozygous males were obtained by crossing the conditional double KO females and B6N males.

The tail tips were used for genotyping. The genotyping primers were purchased from Eurofins Genomics and the primer sequence information is provided in Supplementary Table 7.

Whole-mount immunofluorescence staining. Oocytes and preimplantation embryos were fixed in 3.7% paraformaldehyde (PFA) in PBS containing 0.2% Triton X-100 at room temperature for 20 min. After four washes with PBS containing 10 mg ml^{-1} BSA (PBS/BSA), they were treated with primary antibodies diluted in PBS/BSA at 4 °C overnight. The primary antibodies used in this study were rabbit anti-H2AK119ub1 (1/2,000; Cell Signaling Technology; 8240), mouse anti-H3K27me3 (1/500; Active Motif; 61017) and mouse anti-H3.3 (1/500; Abnova; H00003021-M01). The specificities of the H2AK119ub1 and H3K27me3 antibodies were proven in previous studies that confirmed loss of the immunofluorescence signals in PRC1 and PRC2 KO FGOs, respectively[26,27,56]. After three washes with PBS/BSA, the samples were incubated with a 1:250 dilution of Alexa Fluor 488 donkey anti-mouse IgG and Alexa Fluor 568 donkey anti-rabbit IgG (Life Technologies) at room temperature for 1 h. The samples were washed three times and then mounted on a glass slide in Vectashield antibleaching solution with DAPI (Vector Laboratories). Fluorescence was detected under a Leica TCS SP8 confocal microscope. All images were acquired and quantified using LAS X software (Leica). Briefly, the signal intensity within nuclei of control samples was determined and the cytoplasmic signal was subtracted as background. Then, the averaged signal intensity of the control samples was set as 1.0.

For E6.5 embryos, the embryos were fixed in 3.7% PFA/PBS containing 0.1% Tween-20 at 4 °C overnight. After four washes with PBS containing 0.1% Tween-20, the embryos were incubated with rabbit anti-H3K27me3 (1/1,000; Merck Millipore; 07-449) and goat anti-Oct3/4 (1/1,000; Santa Cruz; sc-8628) at 4 °C for five nights. After four washes with PBS containing 0.1% Tween-20, they were incubated with a 1:500 dilution of Alexa Fluor 568 donkey anti-rabbit IgG and Alexa Fluor 647 donkey anti-goat IgG (Life Technologies) and DAPI at 4 °C for three nights. The samples were washed three times and then mounted on a glass slide in Vectashield antibleaching solution.

RNA-seq. FGOs and F_1 hybrid embryos were prepared as described above. Nineteen FGOs and 7–11 morula embryos per sample were pooled to generate each RNA-seq library. The zona pellucida was removed by brief incubation in acidic Tyrode's solution. E6.5–7.0 embryos for extraembryonic ectoderm dissection were obtained by natural mating with PWK males. The day of the plug was counted as E0.5. Dissection of extraembryonic ectoderm was performed as previously described[27]. To determine the sexes of embryos, the remnants of individual embryos were lysed in proteinase K solution and subjected to PCR with a primer set (*Ube1*-F1 (5′-TGGTCTGGACCCAAACGCTGTCCACA-3′) and *Ube1*-R1 (5′-GGCAGCAGCCATCACATAATCCAGATG-3′)). All samples for RNA-seq were washed three times in 0.2% BSA/PBS before being transferred into a 0.2-ml tube with ~0.5 µl carryover. RNA-seq libraries were prepared as previously described[26]. Briefly, complementary DNA was prepared using a SMART-Seq v4 Ultra Low Input RNA Kit for Sequencing (Takara; 634890) according to the manufacturer's instructions. Library construction was performed on a Nextera XT DNA Library Prep Kit (Illumina; FC-131-1024) with 200 pg complementary DNA, according to the manufacturer's instructions. All RNA-seq libraries were sequenced on a NextSeq 500 (bcl2fastq version 2.17 and RTA version 2.4.11) with single-end 75-bp reads (Illumina).

Whole-mount RNA/DNA FISH. The procedures of the probe preparation and FISH experiment were described previously[28]. Morula embryos were obtained by in vitro fertilization with BDF1 sperm and fixed at 72 h postinsemination. Simultaneous DNA FISH using a bacterial artificial chromosome probe for the *Rnf12* locus on the X chromosome allowed us to distinguish between male and female embryos that had one and two signals in each blastomere, respectively[26,28].

C-section and placental histology. Females were co-caged with B6N males and the presence of plugs was checked on a daily basis. The day of the plug was counted as E0.5. Pregnant females were dissected at E18.5. After counting the numbers of implantation sites and fetuses and measuring the weights of fetuses and placentae, the placentae were fixed in 4% PFA at 4 °C overnight.

The samples were then routinely embedded in paraffin. Serial sections (5 µm thickness) were subjected to hematoxylin and eosin and periodic acid Schiff staining. For the mixed embryo transfer experiment of control and matKO embryos, *Pcgf1/6* control and KO MII oocytes were in vitro fertilized with B6N sperm. After 2 d culture, four- to eight-cell-stage control and matKO embryos were mixed and transferred into surrogate ICR strain mothers. C-section was performed at E19.5.

CUT&RUN data analyses. For CUT&RUN, all sequencing reads after trimming by TrimGalore (version 0.6.4) (https://github.com/FelixKrueger/TrimGalore) and Cutadapt[77] (version 2.8) were aligned to the mouse and *D. melanogaster* genome sequences (mm10 + dm6 for spike-in CUT&RUN; mm10 for general CUT&RUN) using Bowtie 2 (version 2.3.5)[78] with the '-q -N 1 -L 25 --no-mixed --no-discordant' options. For allele-specific analysis of CUT&RUN in the B6 or B6/129 × PWK F_1 hybrid embryos, B6/129 and PWK SNPs were masked as 'N' in the reference genome. After the removal of PCR duplicates using Sambamba[79] with the parameters 'markdup -r -t 2' and filtering out reads with the 'XS' tag, only uniquely mapped reads were used for downstream analysis. SAMtools[80] (version 1.7) was used to manipulate alignments in the SAM and BAM formats. Spike-in normalization was implemented using the exogenous scaling factor computed from the dm6 mapping files (formula used for calculation of scaling factors = 1/(spike-in reads/1,000,000)). For visualization of CUT&RUN using the Integrative Genomics Viewer[81] (version 2.8.0), genome coverage tracks were generated using bamCoverage from deepTools[82] (version 3.3.1) with the parameters '--scaleFactor Scaling_factor --binSize 50 --normalizeUsing RPKM'. SNPsplit[83] (version 0.3.4) was applied to assign uniquely aligned read to its parental origins. To compare replicates, read counts over each bin (5 kilobases (kb)) across the whole genome were calculated and the reads per million values for each bin were used to calculate the Spearman correlation coefficient. Biological replicates were pooled for the visualization and other analyses after validation of the reproducibility (Spearman correlation coefficient > 0.85).

MACS2 (version 2.1.2)[84] was used for peak calling with the parameters '-g mm --nomodel --nolambda --broad'. Following a previous study[18], H2AK119ub1 and H3K27me3 peaks with a distance shorter than 5 kb were merged using the merge function from BEDtools[85] (version 2.26.0) for downstream analysis. Peaks identified in all biological replicates were combined and used for further analysis. When allelic peaks were called by MACS2 using the same parameters as above in each stage, similar numbers of reads (~15 million) were randomly selected to eliminate a potential bias caused by a different sequencing depth. To compare the differential enrichment level in H2AK119ub1 or H3K27me3 from the control group and *Pcgf1/6* matKO group, a set of genomic intervals were generated by combining the overlapping regions of two groups.

RNA-seq data analyses. All RNA-seq reads after trimming using TrimGalore (version 0.6.4) were mapped to the mouse reference genome (mm10) using STAR[86] (version 2.7.3) with default parameters '--runMode alignReads --alignEndsType EndToEnd --outSAMattributes NH NI NM MD --outSAMtype BAM Unsorted'. For allele-specific analysis of B6 or B6/129 × PWK F_1 hybrid embryos, B6/129 and PWK SNPs were masked as 'N' in the reference genome. By filtering the alignment records with the 'NH:i:1' tag and removing duplicates, uniquely aligned reads were used to determine the parental origins. SNPsplit was used to assign the SNP-containing reads to the maternal and paternal genomes.

To identify differentially expressed genes in RNA-seq, raw read counts for each gene were generated using featureCounts[87] (version 1.6.0) with the parameters (-p -s 0 -t exon -g gene_id) and statistical significance was calculated using the edgeR[88] R package (version 3.28.0). For comparative expression analysis in two conditions or two alleles, RPKM and $\log_2$[fold changes] of specific genes were used. The RPKM values of each gene were generated using RSEM[89] (version 1.3.1) to visualize the correlation analyses between biological replicates and compute the Pearson correlation coefficient.

Analysis of H2AK119ub dynamics. To visualize the read density at regions of interest, computeMatrix, plotHeatmap and plotProfile from the deepTools suite (version 3.3.1) were used to display heatmaps and metaplots. To display the profiles across all developmental stages, a set of H2AK119ub1 peaks was generated by merging peaks across stages. For the enrichment analysis at specific regions in different developmental stages, the read coverage in 50-bp bins was calculated and *z* score normalization was performed at each bin within peak regions according to a previous study[18]. *K*-means clustering was performed using deepTools (version 3.3.1) with $k = 3$. Rows were ordered within each cluster by the mean normalized enrichment values. The above method was also used to facilitate clustering of H2AK119ub1 enrichment level in promoters and gene body regions across stages, as well as the combination of H2AK119ub1, H3K27me3 and H3K4me3 for analyses of FGOs.

Hierarchical clustering analysis. To measure the distance between maternal and paternal H2AK119ub1 enrichment levels in different developmental stages, a hierarchical clustering analysis was conducted using the R package ape and the R function hclust, according to a previous study[18]. The average RPKM within a 5-kb window across the entire genome was calculated to compute the distance by (1 − Spearman's correlation).

Analysis of the correlation between H2AK119ub1 enrichment and gene density. To characterize the relationship between H2AK119ub1 enrichment and gene density, 1-Mb sliding windows with a 2-kb step across the mouse genome were generated using the makewindows function in BEDtools. The NCBI RefSeq gene annotation databases were used to calculate the number of genes in the window. RPKM values of each window were calculated. For correlation analysis, LOESS was used as smoothing method with a 95% confidence interval between the H2AK119ub1 enrichment level and gene density. To display the gene density heatmap, the minimum gene count in a 1-Mb sliding window (with a 2-kb step) that contained the corresponding H2AK119ub1 peak was shown. A 1-Mb sliding window with ≤1 gene was defined as the gene desert.

Definition of PMDs. The identification of PMDs was performed similarly, as previously described[90]. Briefly, 1-Mb sliding windows over the entire genome were selected and the average DNA methylation levels of the window were computed. Only those windows in which the average DNA methylation levels were <0.6 and the number of CpGs was more than 20 were considered as PMDs.

Genomic distribution of CUT&RUN peaks. To identify the genomic features of CUT&RUN peaks, the peaks were annotated with the priority order (promoter > exon > intron > downstream > intergenic) using ChIPseeker[91] (version 1.22.1) when a single peak spanned more than two genomic features. The promoter and downstream were defined as the transcription start site ± 2.5 kb and transcription end site + 3 kb, respectively.

Typical Polycomb target genes. The 1,797 typical Polycomb target genes were defined by S. Ito et al. (manuscript in preparation). Briefly, these genes were the top lists of genes highly enriched with SUZ12, KDM2B and RING1B at CpG islands located at their transcription start sites in mESCs.

Statistical analyses. To determine statistically significant differences in allelic expression levels between chromosome X and other chromosomes, one-way analysis of variance was used in R (www.r-project.org/). In addition, GeneOverlap (version 1.23.0; http://shenlab-sinai.github.io/shenlab-sinai/), a Bioconductor package, was used to perform a Fisher's exact test of whether two variables were independent.

Reporting Summary. Further information on research design is available in the Nature Research Reporting Summary linked to this article.

Data availability

All of the CUT&RUN and RNA-seq datasets generated in this study are summarized in Supplementary Table 6 and have been deposited to the Gene Expression Omnibus database under accession number GSE153496. The H2AK119ub1 ChIP-seq datasets of mESCs were from GSE119620 (ref. [41]). The H3K27me3 and H3K4me3 ChIP-seq and whole-genome bisulfite sequencing datasets of FGOs were from GSE93941 (ref. [19]). The H3K27me3 ChIP-seq datasets of 7-d GOs, MII oocytes, zygotes, early two-cell embryos, late two-cell embryos, inner cell masses of blastocysts and E6.5 epiblasts were from GSE76687 (ref. [18]). The H3K27me3 CUT&RUN datasets of morula embryos were from GSE116713 (ref. [26]). The H3K27me3 ChIP-seq datasets in mESCs were from GSE119620 (ref. [41]). The RNA-seq datasets of *Ring1a/1b* KO FGOs and *Dnmt3l* matKO and *Eed* matKO morula embryos were from GSE132156 (ref. [56]), GSE130115 (ref. [29]) and GSE116713 (ref. [26]), respectively. The PCGF1 ChIP-seq datasets in mESCs were from GSE119620 (ref. [41]).

Code availability

The code developed for this study is available at https://github.com/Azusa-lab/Intergenerational-epigenetic-inheritance.

References

77. Martin, M. Cutadapt removes adapter sequences from high-throughput sequencing reads. *EMBnet. J.* **17**, 10–12 (2011).
78. Langmead, B. & Salzberg, S. L. Fast gapped-read alignment with Bowtie 2. *Nat. Methods* **9**, 357–359 (2012).
79. Tarasov, A., Vilella, A. J., Cuppen, E., Nijman, I. J. & Prins, P. Sambamba: fast processing of NGS alignment formats. *Bioinformatics* **31**, 2032–2034 (2015).
80. Li, H. et al. The Sequence Alignment/Map format and SAMtools. *Bioinformatics* **25**, 2078–2079 (2009).
81. Robinson, J. et al. Integrative Genomics Viewer. *Nat. Biotechnol.* **29**, 24–26 (2011).
82. Ramirez, F., Dündar, F., Diehl, S., Grüning, B. A. & Manke, T. deepTools: a flexible platform for exploring deep-sequencing data. *Nucleic Acids Res.* **42**, W187–W191 (2014).

83. Krueger, F. & Andrews, S. R. SNPsplit: allele-specific splitting of alignments between genomes with known SNP genotypes. *F1000Res* **5**, 1479 (2016).
84. Zhang, Y. et al. Model-based analysis of ChIP-Seq (MACS). *Genome Biol.* **9**, R137 (2008).
85. Quinlan, A. R. & Hall, I. M. BEDTools: a flexible suite of utilities for comparing genomic features. *Bioinformatics* **26**, 841–842 (2010).
86. Dobin, A. et al. STAR: ultrafast universal RNA-seq aligner. *Bioinformatics* **29**, 15–21 (2013).
87. Liao, Y., Smyth, G. K. & Shi, W. featureCounts: an efficient general purpose program for assigning sequence reads to genomic features. *Bioinformatics* **30**, 923–930 (2014).
88. Robinson, M. D., McCarthy, D. J. & Smyth, G. K. edgeR: a Bioconductor package for differential expression analysis of digital gene expression data. *Bioinformatics* **26**, 139–140 (2010).
89. Li, B. & Dewey, C. N. RSEM: accurate transcript quantification from RNA-Seq data with or without a reference genome. *BMC Bioinformatics* **12**, 323 (2011).
90. Lister, R. et al. Human DNA methylomes at base resolution show widespread epigenomic differences. *Nature* **462**, 315–322 (2009).
91. Yu, G., Wang, L.-G. & He, Q.-Y. ChIPseeker: an R/Bioconductor package for ChIP peak annotation, comparison and visualization. *Bioinformatics* **31**, 2382–2383 (2015).

Acknowledgements

We thank all of the Koseki laboratory members for helpful discussion and the Kazusa DNA Research Institute for support with next-generation sequencing. The protein A-MNase for CUT&RUN was a kind gift from S. Henikoff. We appreciate T. Ishiuchi (Kyushu University), S. Ito (RIKEN) and S. Yamaguchi (Osaka University) for critical reading of the manuscript and K. Yamamoto and T. Yamamoto (RIKEN) for support as the young chief investigator program directors. This project was partly supported by the Ministry of Education, Culture, Sports, Science and Technology (MEXT) Leading Initiative for Excellent Young Researchers Grant (to A.I.), Japan Society for the Promotion of Science (JSPS) Grants-in-Aid for Scientific Research (KAKENHI) (18H02359 to A.I. and 16H02622 to H.K.), Grants-in-Aid for Scientific Research on Innovative Areas (19H05754 to A.I. and 19H05745 to H.K.), Grant-in-Aid for Early-Career Scientists (19K17971 to C.K.), Grant-in-Aid for JSPS Fellows (20J21541 to R.H.), Japan Agency for Medical Research and Development (PRIME; JP18gm6110012 to A.I.), AMED-CREST (JP18gm0510016 to H.K.), the Uehara Memorial Foundation (to A.I.) and intramural grants within RIKEN, including the All-RIKEN 'Epigenome Manipulation Project' (to A.I. and H.K.).

Author contributions

A.I. conceived the project and designed the experiments. H.M. analyzed the sequencing data. A.I., C.K., R.H. and M.K. performed the experiments. R.H. helped with the data analysis. A.I. and H.M. interpreted the data. H.K. provided the *Pcgf1* and *Pcgf6* floxed mouse lines. A.I. and H.M. wrote the manuscript with contributions from H.K.

Competing interests

The authors declare no competing interests.

Additional information

Extended data is available for this paper at https://doi.org/10.1038/s41588-021-00820-3.

Supplementary information The online version contains supplementary material available at https://doi.org/10.1038/s41588-021-00820-3.

Correspondence and requests for materials should be addressed to A.I.

Peer review information *Nature Genetics* thanks Neil Brockdorff, Maxim Greenberg and the other, anonymous, reviewer(s) for their contribution to the peer review of this work.

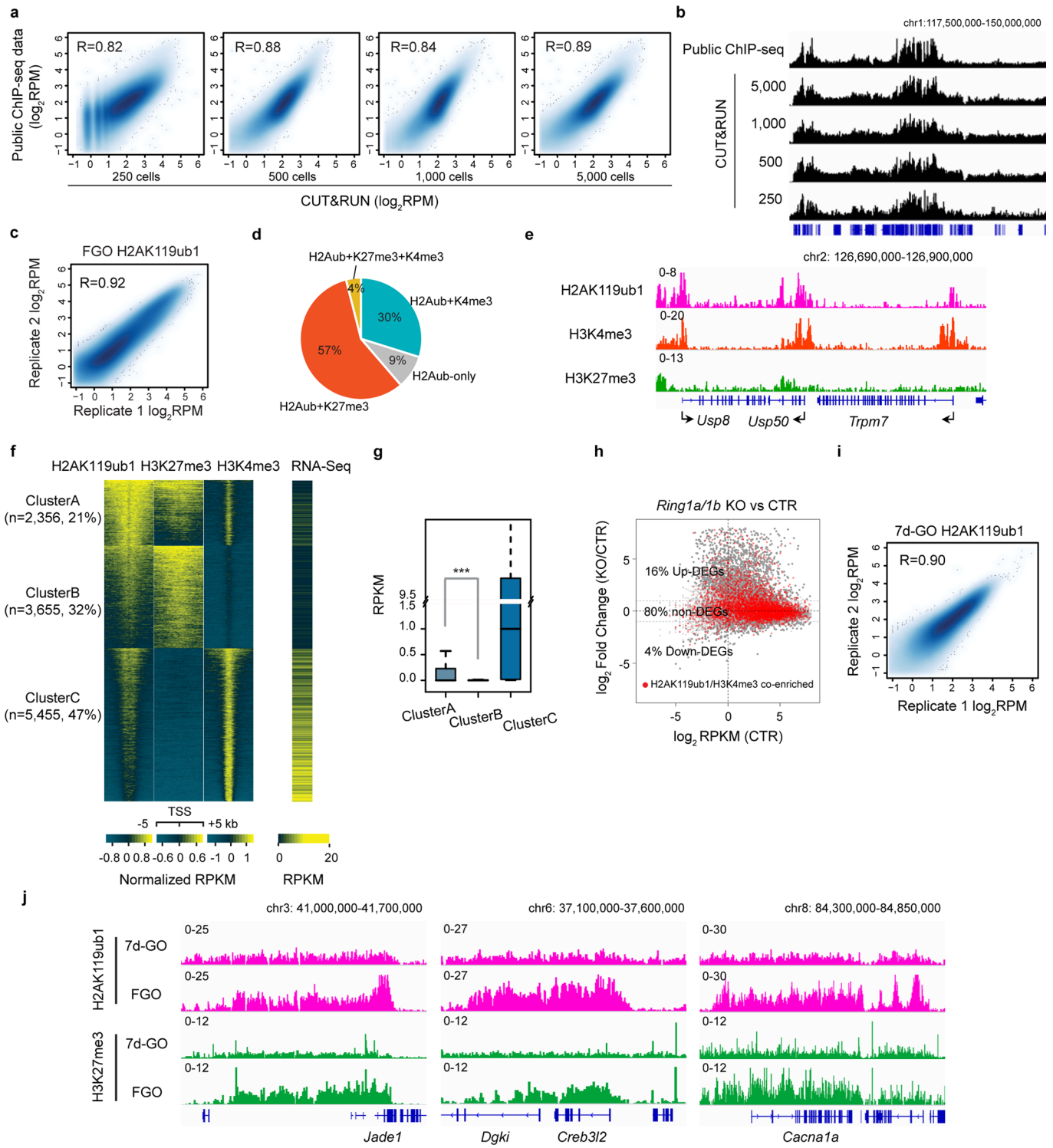

Extended Data Fig. 1 | See next page for caption.

Extended Data Fig. 1 | Characterization of H2AK119ub1 distribution in mouse oocytes. a, Scatter plots showing H2AK119ub1 enrichment (10 kb window) between our low-input CUT&RUN datasets using 250, 500, 1,000, 5,000 mouse embryonic stem cells (mESCs) and a public ChIP-seq dataset in mESCs[41]. Spearman correlation is also shown. **b**, Genome browser view of H2AK119ub1 in our low-input CUT&RUN datasets and a public ChIP-seq dataset of mESCs. **c**, Scatter plot showing the correlation between biological duplicate of H2AK119ub1 CUT&RUN in FGOs. **d**, Pie chart showing the percentage of H2AK119ub1 (H2Aub)-covered regions that overlap H3K27me3 (K27me3) or/and H3K4me3 (K4me3). **e**, Genome browser view showing local association of H2AK119ub1 and H3K4me3 at promoters in FGOs. The H3K4me3 and H3K27me3 ChIP-seq datasets are from[19]. **f**, Heatmap showing the enrichment of H2AK119ub1, H3K27me3, and H3K4me3 at promoters harboring H2AK119ub1 peaks in FGOs. Reads density (normalized RPKM with different scales) are plotted at ±5 kb of the transcription start sites (TSS). The promoters are clustered into 3 groups according to the relative enrichment of the histone PTMs. The H3K27me3 and H3K4me3 ChIP-seq datasets are from[19]. The rightmost column represents the expression levels of genes corresponding to individual rows in FGOs. The RNA-seq dataset is from[16]. **g**, Box plot showing gene expression levels of the 3 clusters of panel **f**. The middle lines in the boxes represent the medians. Box edges, the upper, and the lower whiskers indicate the interquartile range (IQR, from the 25th to 75th percentile), the largest value smaller than 1.5 x IQR above the 75th percentile, and the smallest value larger than 1.5 x IQR below the 25th percentile, respectively (n = 1, as biological replicates were combined). *** *p*-value = 1.43e-71 (two sided Mann-Whitney *U* test). **h**, MA plot of log2FC(KO/CTR) in gene expression of *Ring1a/1b* KO FGOs. Cluster C genes in panel **f** are highlighted by red dots. The percentages of up- and down-regulated differentially expressed genes (DEGs) and non-DEGs with the fold change>2 cutoff are indicated. **i**, Scatter plot showing the correlation between biological duplicates of H2AK119ub1 CUT&RUN in 7d-GOs. **j**, Additional genome browser views of H2AK119ub1 and H3K27me3 distributions in 7d-GOs and FGOs. The H3K27me3 ChIP-seq datasets are from[18].

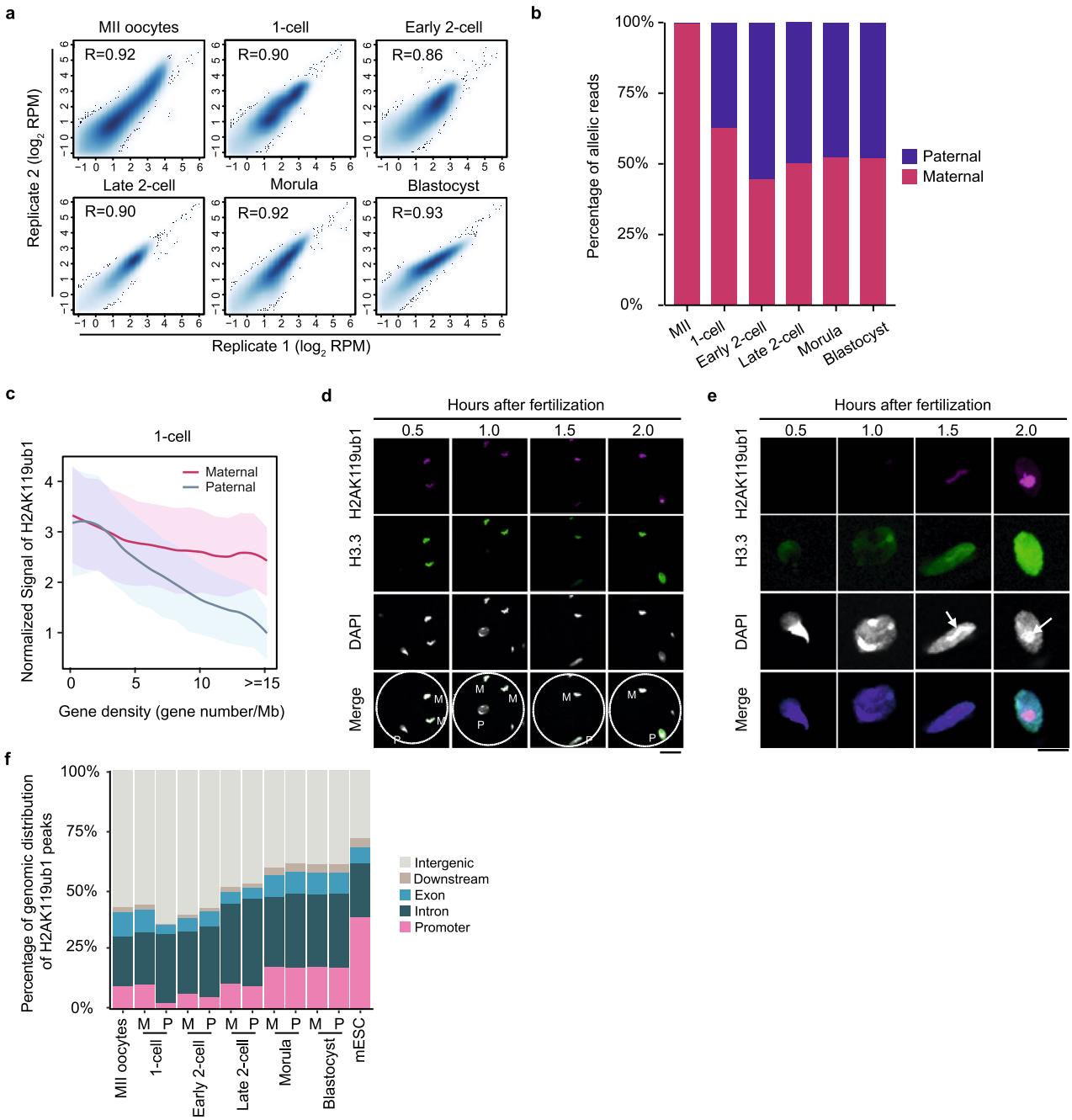

Extended Data Fig. 2 | Characterization of allelic H2AK119ub1 distribution at the maternal-to-zygotic transition. a, Scatter plot showing the correlations between biological duplicates of H2AK119ub1 CUT&RUN in individual samples. **b**, The ratios of SNP-containing reads assigned to the paternal and maternal genomes. Note that MII oocytes have almost no paternal SNP reads, supporting the validity of our SNP analysis pipeline. **c**, Averaged signal profiles of H2AK119ub1 at regions with different gene densities (gene number per 1 Mb sliding window with a 2kb step) in zygotes (n=1, as biological replicates were combined). The shaded areas represent the 95% confidence interval for the fitted LOESS curve. Note that the H2AK119ub1 enrichment at the paternal allele is negatively correlated with gene density. **d**, Representative images of anti-H2AK119ub1 and anti-H3.3 immunostaining analysis for fertilized oocytes. Dotted circles, the rims of fertilized oocytes. M, maternal genome. P, paternal genome. Scale bar, 20 μm. Ten fertilized oocytes were examined in each time point. **e**, Enlarged images of the paternal genomes in panel **d**. DAPI-dense loci are pointed by arrows. DAPI was shown in blue in the merged images. Scale bar, 10 μm. **f**, Genomic distribution of H2AK119ub1 peaks. M, maternal allele. P, paternal allele. Promoters represent the regions of ±2.5 kb around transcription start sites.

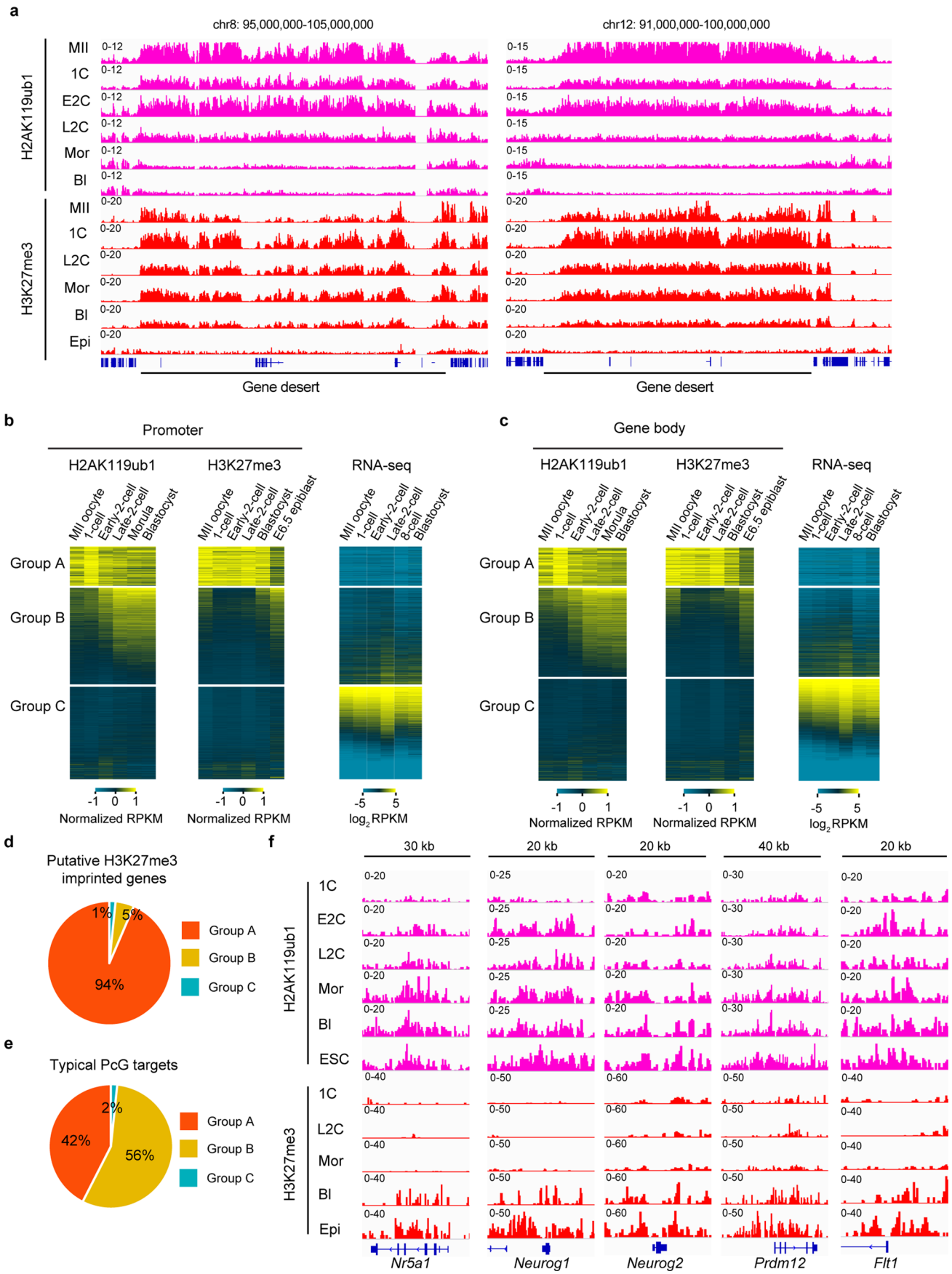

Extended Data Fig. 3 | See next page for caption.

Extended Data Fig. 3 | H2AK119ub1 dynamics and gene expression during the maternal-to-zygotic transition. a, Genome browser views of H2AK119ub1 and H3K27me3 dynamics at gene deserts. MII, MII oocyte. 1C, 1-cell. E2C, early 2-cell. L2C, late 2-cell. Mor, morula. Bl, blastocyst. Epi, E6.5 epiblast. **b, c**, Heatmaps showing the H2AK119ub1 and H3K27me3 enrichment at promoters (**b**) and gene bodies (**c**) in the maternal allele of the indicated samples. Genes with few SNP reads [RPKM(H2AK119ub1) < 1 in all samples] were filtered out from this analysis. The gene expression levels are shown in the right RNA-seq heatmap. The H3K27me3 ChIP-seq datasets are from[18]. The RNA-seq datasets are from[16]. **d**, Pie chart showing the proportion of putative H3K27me3-dependent imprinted genes[27] in Group A/B/C of the panel **c**. Genes with few SNP reads [RPKM(H2AK119ub1) < 1 in all samples] were filtered out from this analysis. The total number of genes in this pie chart is 62. **e**, Pie chart showing the proportion of typical Polycomb (PcG) target genes in Group A/B/C of the panel **b**. Genes with few SNP reads [RPKM(H2AK119ub1) < 1 in all samples] were filtered out from this analysis. The total number of genes in this pie chart is 1,405. **f**, Genome browser views of H2AK119ub1 and H3K27me3 dynamics at typical PcG targets. The genomic length of each view is indicated at the top. ESC, embryonic stem cells.

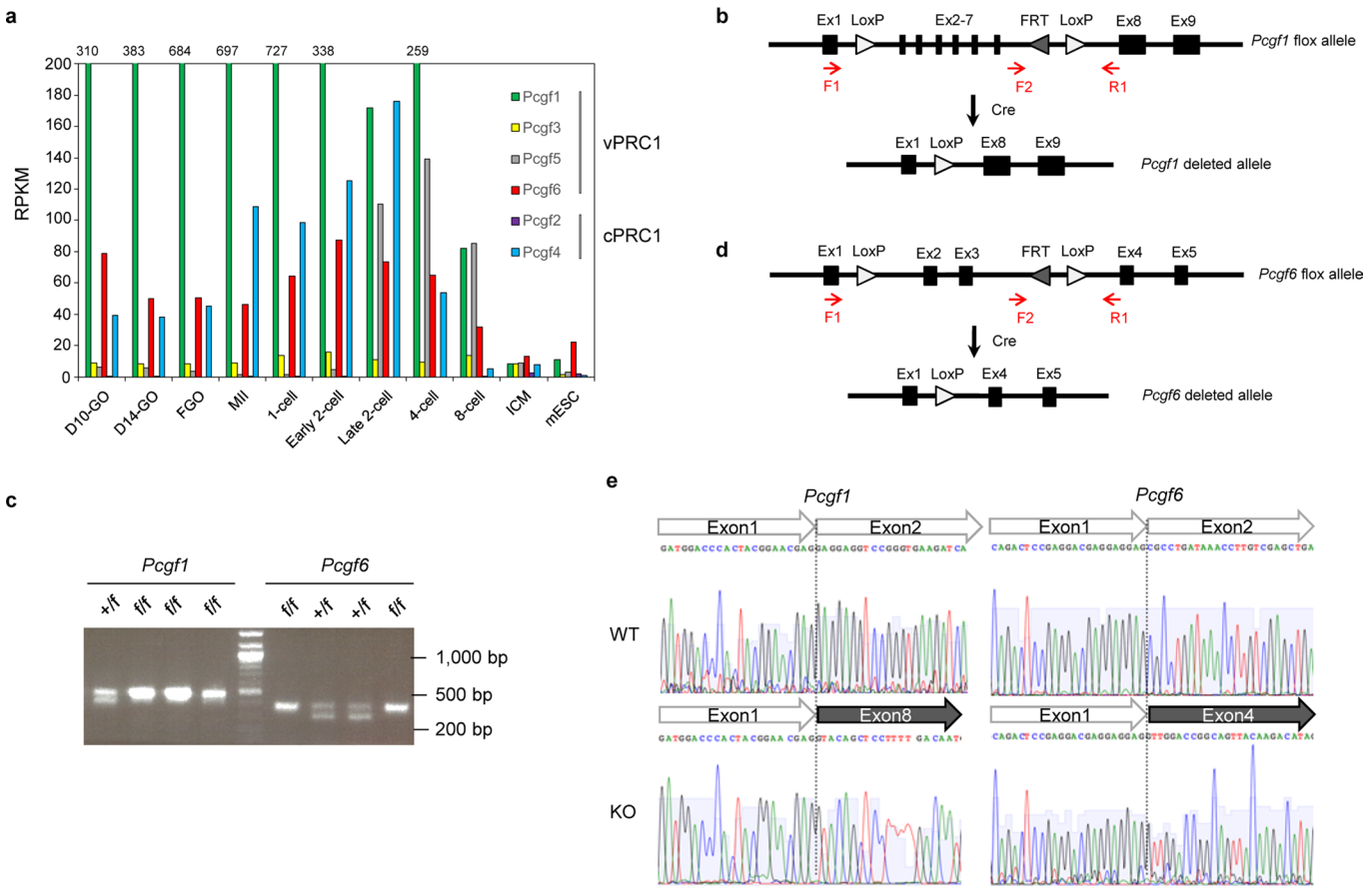

Extended Data Fig. 4 | Generation of oocyte-specific *Pcgf1/6* knockout mice. a, The expression levels of the *Pcgf* family genes during oogenesis and preimplantation development. The RNA-seq datasets are from[16]. The exact RPKM values of *Pcgf1* over 200 are indicated at the top of the bars. D10-and D14-GO, growing oocytes (GO) from postnatal day 10 (D10) and day 14 (D14) females. FGO, fully-grown oocytes. MII, MII-stage oocytes. ICM, inner cell mass of blastocysts. mESC, mouse embryonic stem cell. vPRC1, variant PRC1 components. cPRC1, canonical PRC1 components. **b**, Construct for targeted disruption of *Pcgf1*. Black boxes indicate the coding exons. Red arrows indicate genotyping primers. **c**, Genotyping of *Pcgf1* and *Pcgf6* flox alleles. The F2/R1 primer set was used to detect WT and flox alleles. **d**, Construct for targeted disruption of *Pcgf6*. **e**, Sanger sequencing to confirm the deletions of floxed exons in *Pcgf1/6* KO FGOs. After cDNA preparation by reverse transcription of total RNA from WT or KO FGOs, the targeted regions were PCR amplified and sequenced. This confirmed that exons 2–7 (*Pcgf1*) and 2–3 (*Pcgf6*), which encode the Ring finger domains of PCGF1 and PCGF6, respectively, were successfully deleted in KO FGOs.

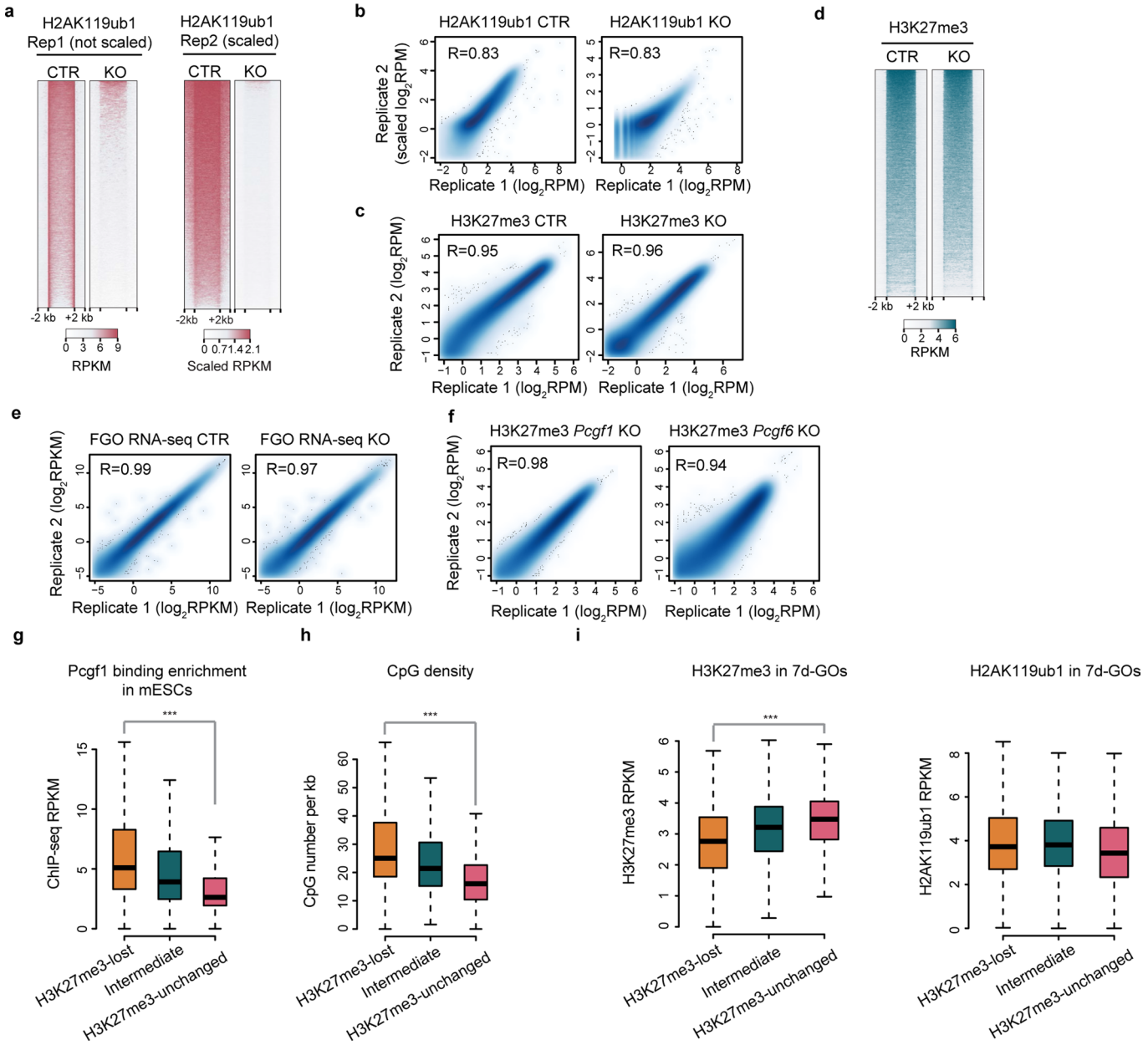

Extended Data Fig. 5 | Characterization of *Pcgf1/6* KO fully-grown oocytes (FGOs). a, Heatmap showing the enrichment of H2AK119ub1 CUT&RUN signals in replicate 1 (not scaled) and 2 (scaled by spike-in chromatin). Reads densities are plotted at the peaks ±2 kb flanking regions. **b, c**, Scatter plots showing the correlations between biological duplicates of H2AK119ub1 (**b**) and H3K27me3 (**c**) CUT&RUN in CTR and KO FGOs. **d**, Heatmap showing the enrichment of H3K27me3 CUT&RUN signals. Reads density are plotted at the peaks ±2 kb flanking regions. **e**, Scatter plots showing the correlations between biological duplicates of RNA-seq in CTR and KO FGOs. **f**, Scatter plots showing the correlations between biological duplicates of H3K27me3 CUT&RUN in *Pcgf1* and *Pcgf6* single KO FGOs. **g**, Box plot showing the enrichment of PCGF1 binding at H3K27me3-lost, -intermediate, and -unchanged genes defined in Fig. 4e. PCGF1 ChIP-seq datasets in mESCs are from[41]. ***$p = 1.8e\text{-}105$ (two sided Mann-Whitney *U* test). **h**, Box plot showing CpG density at promoters of the 3 groups of genes. ***$p = 3.9e\text{-}100$ (two sided Mann-Whitney *U* test). **i**, Box plot showing H2AK119ub1 and H3K27me3 enrichment at gene bodies of the 3 groups in 7-day growing oocytes (7d-GOs). ***$p = 2.3e\text{-}69$ (two sided Mann-Whitney *U* test).

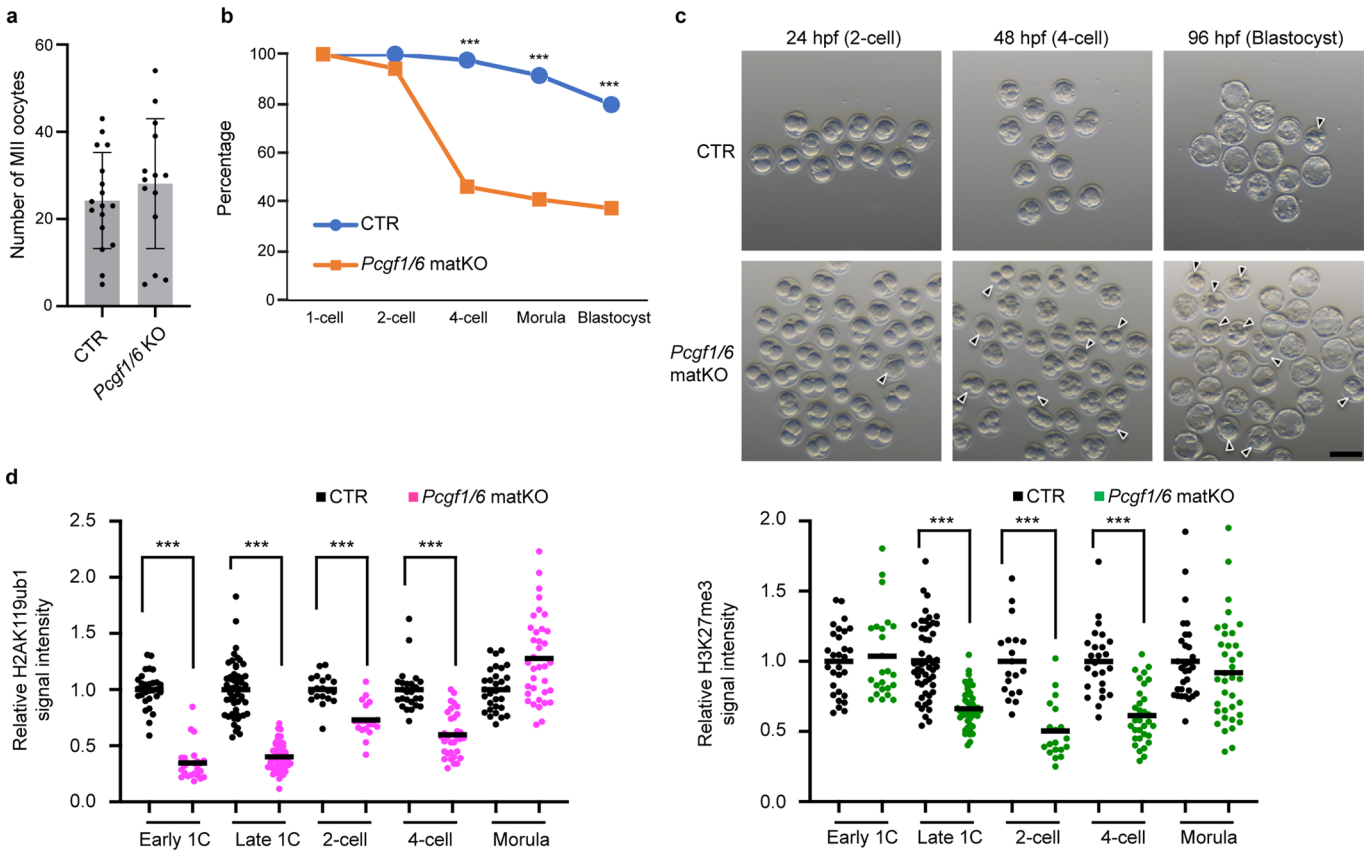

Extended Data Fig. 6 | Preimplantation development of *Pcgf1/6* maternal KO (matKO) embryos. a, The averaged numbers of MII oocytes following superovulation. The numbers of females examined were 17 (CTR) and 14 (KO). Error bars, SD. **b**, Preimplantation development of *Pcgf1/6* CTR and matKO embryos. The embryos that reached at the 2-cell, 4-cell, morula, and blastocyst stages in a timely fashion were counted at 24, 48, 72, and 96 hours post-fertilization (hpf), respectively. The numbers of 1-cell zygotes were set as 100%. The numbers of embryos examined are 127 (CTR) and 171 (matKO) from 6 biologically independent experiments. ***$p < 0.001$ (Chi-squired test). **c**, Representative images of preimplantation embryos at the indicated time points. The expected stages at these time points are indicated in parentheses. The arrowheads indicate embryos that had not reached the expected stages in a timely manner. Note that the other *Pcgf1/6* matKO embryos form grossly normal blastocysts at 96 hpf. The experiment was repeated 6 times. Scale bar, 100 μm. **d**, Quantifications of H2AK119ub1 and H3K27me3 immunostaining analysis in *Pcgf1/6* CTR and matKO embryos. The numbers of embryos examined (n) are indicated in Fig. 5a. The averaged signal intensity of CTR was set as 1.0 in each stage. Maternal pronuclei were quantified for 1-cell zygotes. Bars overlaid on the plots indicate mean. ***$p < 0.001$ (two-tailed Student's *t*-test).

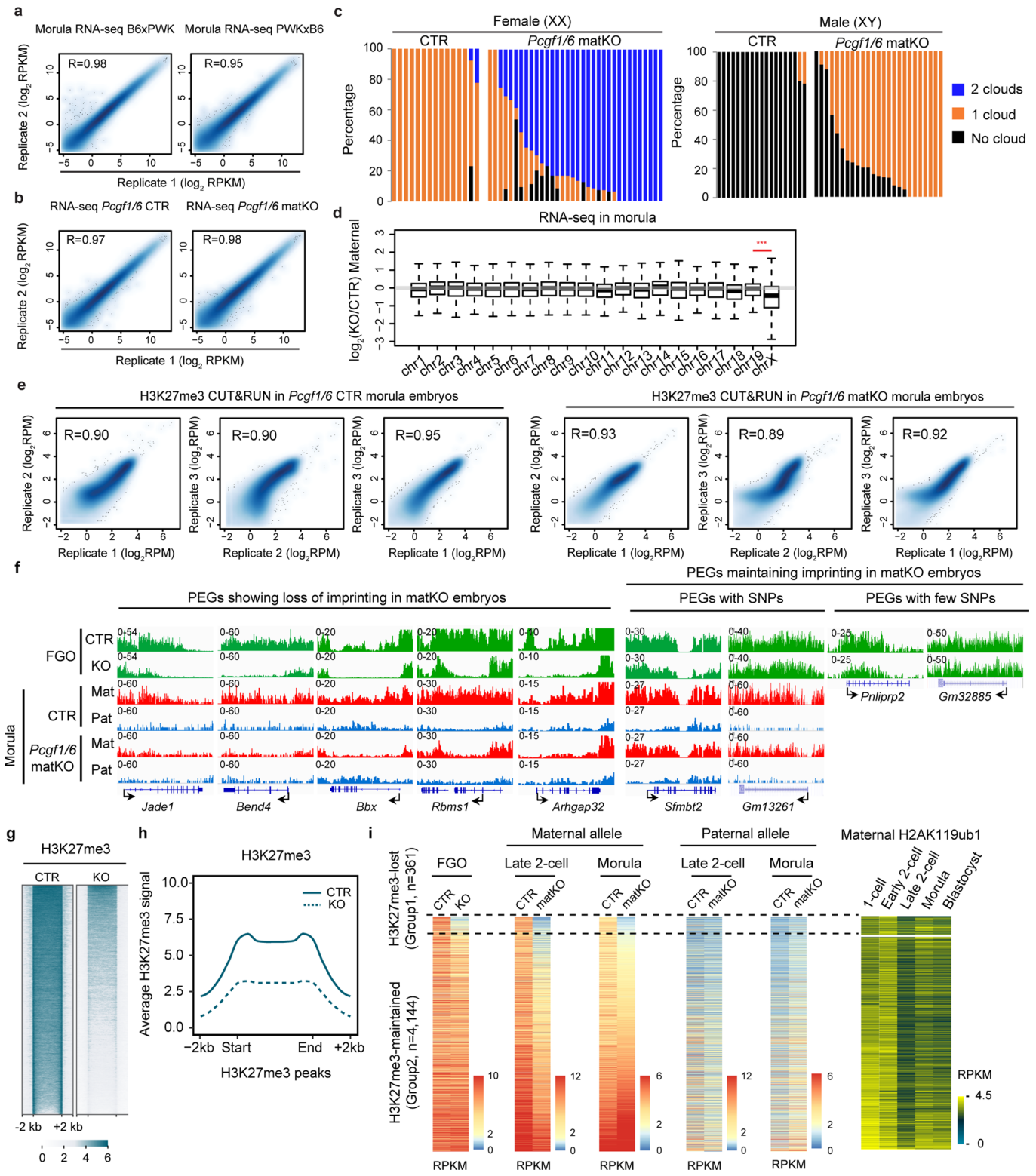

Extended Data Fig. 7 | See next page for caption.

Extended Data Fig. 7 | Characterization of *Pcgf1/6* maternal KO (matKO) morula embryos. a, b, Scatter plots showing the correlations between biological duplicates of RNA-seq in B6xPWK and PWKxB6 (**a**) and *Pcgf1/6* CTR and matKO (**b**) morula embryos. **c**, The ratio of blastomeres showing the indicated numbers of *Xist* RNA clouds. Each bar represents an individual embryo. **d**, Box plot showing the relative expression of genes on individual maternal chromosomes between CTR and matKO morula embryos. Box edges, the upper, and the lower whiskers indicate the interquartile range (IQR, from the 25th to 75th percentile), the largest value smaller than 1.5 x IQR above the 75th percentile, and the smallest value larger than 1.5 x IQR below the 25th percentile, respectively (n=1, as biological replicates were combined). ***$p < 2.2e\text{-}16$ (One-way ANOVA test). **e**, Scatter plots showing the correlations between biological triplicates of H3K27me3 CUT&RUN in CTR and matKO morula embryos. **f**, Additional genome browser views of H3K27me3 distributions in *Pcgf1/6* CTR and KO FGOs, and CTR and matKO morula embryos. Mat, maternal allele. Pat, paternal allele. No views in embryos are shown at *Pnliprp2* and *Gm32885* that have few SNPs. **g**, Heatmap showing the CUT&RUN signal enrichment of maternal H3K27me3 (scaled) in late 2-cell embryos. Reads density were plotted at the peaks ±2 kb flanking regions. **h**, Averaged signal profiles of maternal H3K27me3 (scaled) at their peaks ±2 kb flanking regions in late 2-cell embryos. **i**, Heatmap showing the enrichment of the H3K27me3 intensity in FGOs, late 2-cell, and morula embryos. The list and the order of genes are the same as Fig. 5d. Heatmaps for the corresponding paternal allele are also shown. The rightmost heatmap indicates H2AK119ub1 signal intensity at the maternal allele of wild-type preimplantation embryos.

a

Mother	Father	No. of litters	No. of Implantation (Ave ± SD)	No. of embryos (Ave ± SD)	Embryo/Implantation
Pcgf1$^{f/f}$, Pcgf6$^{f/f}$	WT (B6)	4	35 (8.8±0.5)	32 (8.0±0.8)	32/35 (91%)
Zp3-Cre, Pcgf1$^{f/f}$, Pcgf6$^{f/f}$	WT (B6)	8	30 (3.8±2.3)	15 (1.9±1.0)	15/30 (50%)

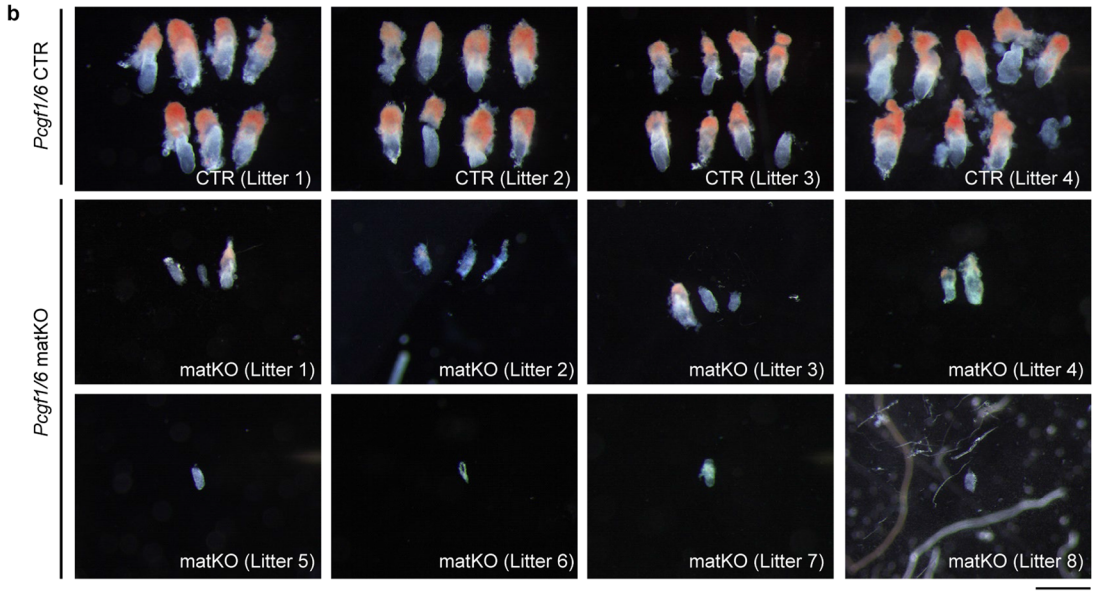

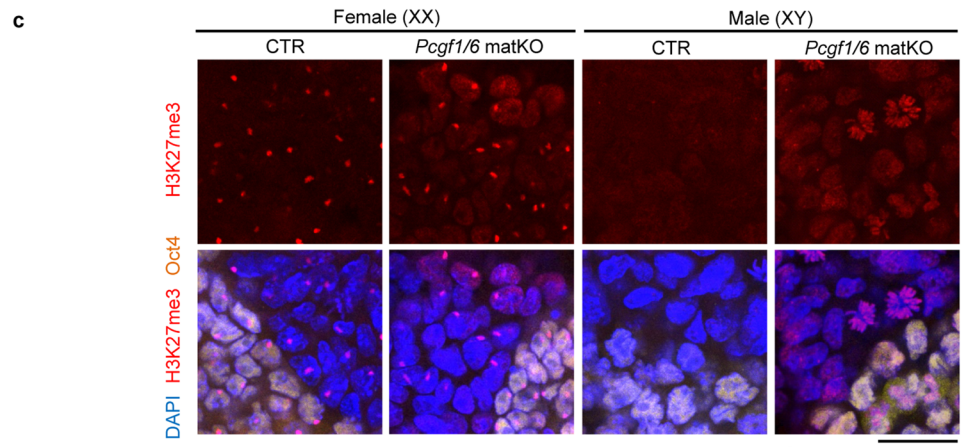

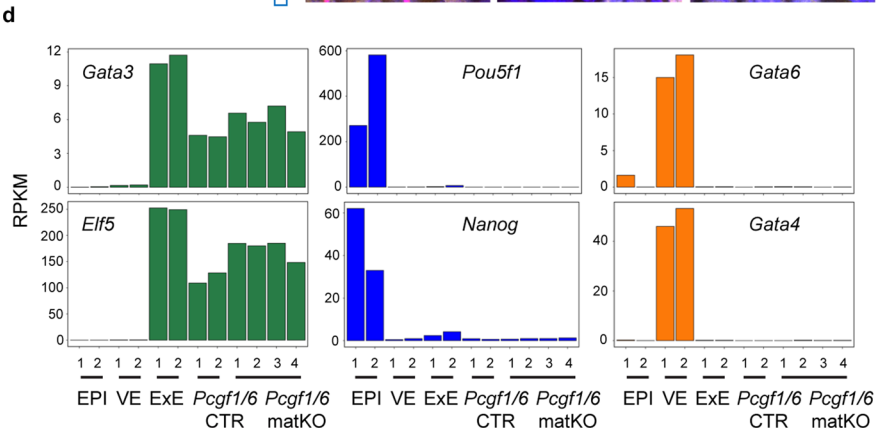

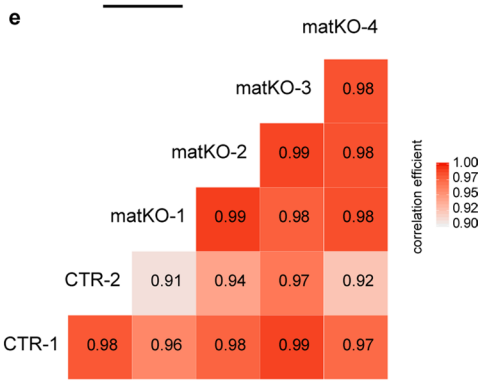

Extended Data Fig. 8 | See next page for caption.

Extended Data Fig. 8 | Characterization of *Pcgf1/6* maternal KO (matKO) embryos at E6.5. a, Summary table of E6.5 dissection. **b**, Pictures of all of 4 CTR and 8 matKO litters at E6.5. Scale bar, 1 mm. **c**, Representative images of H3K27me3 immunostaining of E6.5 embryos. H3K27me3 spots are indicators of X chromosome inactivation (XCI). Note that single XCI and no XCI is observed in female and male embryos, respectively, in both CTR and matKO. This indicates that aberrant XCI in matKO embryos is restored by E6.5. Oct4-positive and -negative cells represent epiblast and extra-embryonic ectoderm, respectively. The number of embryos examined was 6 (CTR) and 9 (matKO) females and 9 (CTR) and 5 (matKO) males. Scale bar, 50 μm. **d**, Expression levels of cell lineage marker genes in CTR and matKO extraembryonic ectoderm (ExE) samples. RNA-seq datasets of wild-type epiblast (EPI), visceral endoderm (VE), and ExEs are from[27]. **e**, Correlation between biological replicates of RNA-seq samples.

a

Mother	Father	No. of litters	No. of Implantation (Ave±SD)	No. of live fetuses (Ave±SD)	Fetus/ Implantation	Placental weight (mg) (Ave±SD)	Fetal weight (g) (Ave±SD)
Pcgf1$^{f/f}$, Pcgf6$^{f/f}$	WT (B6)	11	89 (8.1±1.2)	85 (7.7±1.0)	85/89 (96%)	78.9±12.7	1.13±0.12
Zp3-Cre, Pcgf1$^{f/f}$, Pcgf6$^{f/f}$	WT (B6)	10	44 (4.4±1.6)	24 (2.4±1.2)	24/44 (55%)	136.6±24.4	1.10±0.16

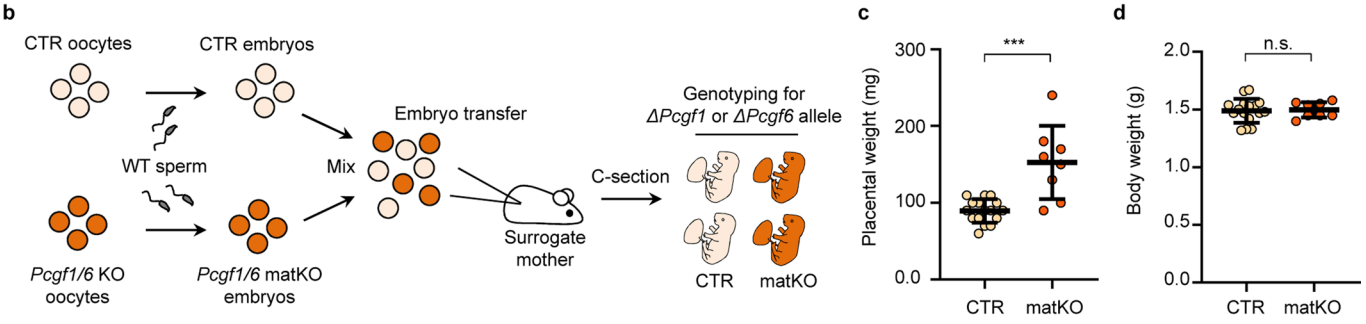

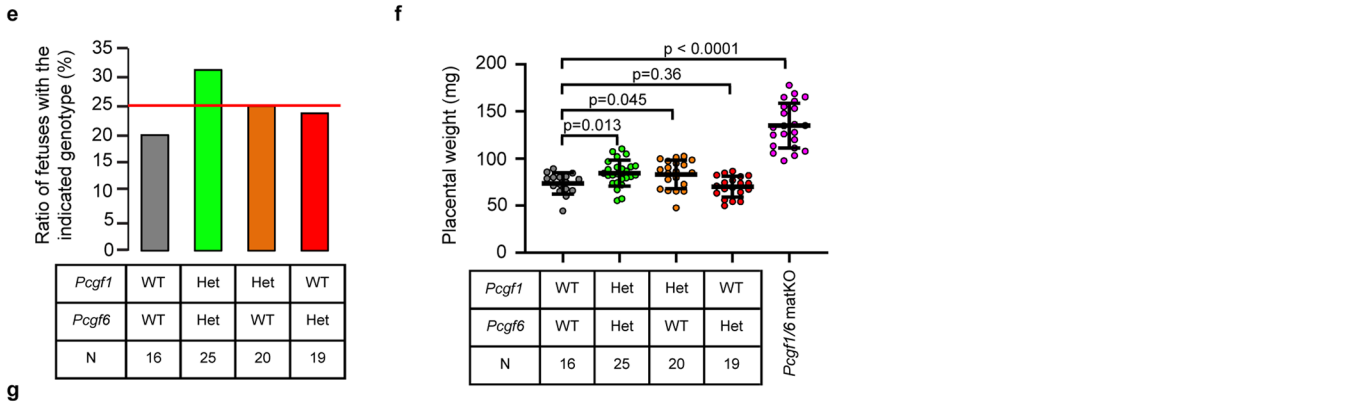

g

Mother	Father	No. of litters	No. of Implantation (Ave±SD)	No. of live fetuses (Ave±SD)	Fetus/ Implantation	Placental weight (mg) (Ave±SD)	Fetal weight (g) (Ave±SD)
Zp3-Cre, Pcgf1$^{f/f}$ *	WT (B6)	7	56 (8.0±1.0)	48 (6.9±1.5)	48/56 (86%)	99.1±18.1	1.11±0.12
Zp3-Cre, Pcgf6$^{f/f}$ **	WT (B6)	10	73 (7.3±2.2)	69 (6.9±2.6)	69/73 (95%)	92.6±17.5	1.19±0.16

* The *Pcgf6* allele is +/+ or +/f.
** The *Pcgf1* allele is +/+ or +/f.

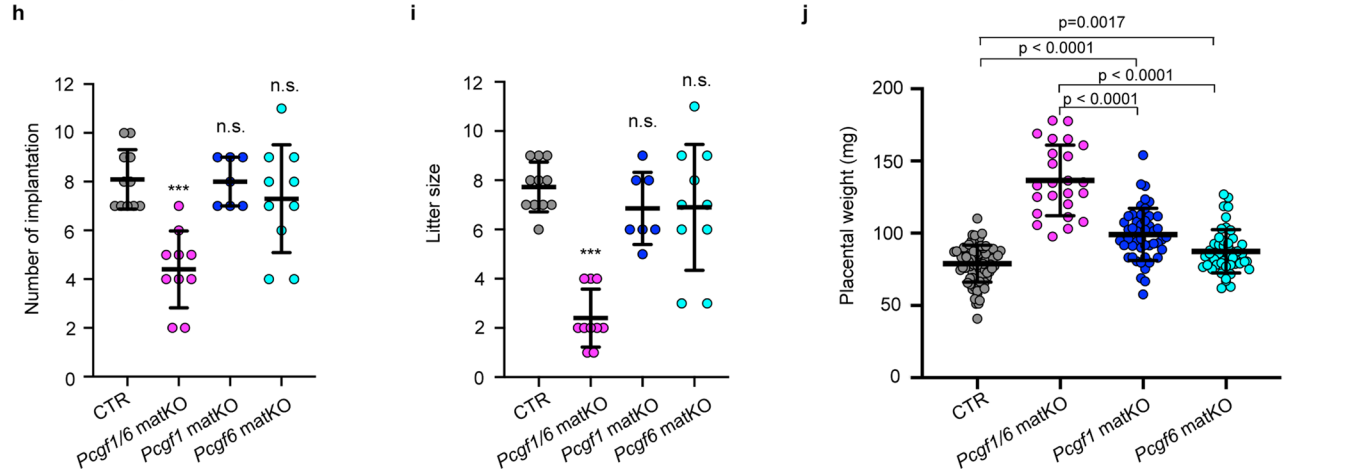

Extended Data Fig. 9 | See next page for caption.

Extended Data Fig. 9 | Characterization of *Pcgf1/6* double and respective single maternal KO (matKO) fetuses and placentae at term. a, Summary table of Caesarean sections at E18.5. **b**, Experimental scheme of mixed embryo transfer. Genotyping of the *ΔPcgf1* or *ΔPcgf6* allele allows distinguishing between CTR and matKO fetuses. **c, d**, Placental weights (**c**) and body weights (**d**) of *Pcgf1/6* CTR and matKO fetuses dissected from surrogated mothers at E19.5. Bars overlaid on the plots indicate mean±SD. The number of placentae and fetuses examined was 16 (CTR) and 8 (matKO) from 3 litters. ***$p < 0.0001$ (two-tailed Student's *t*-test). **e**, Ratios of wild-type (WT), *Pcgf1* heterozygous (Het), *Pcgf6* Het, *Pcgf1/6* double Het fetuses derived from WT females that had been mated with *Pcgf1/6* double Het males. A total of 80 fetuses obtained from 9 litters were examined at E18.5. **f**, Placental weights of the indicated genotypes. Bars overlaid on the plots indicate mean±SD. *p*, two-tailed Student's *t*-test. **g**, Summary table of Caesarean sections at E18.5 for *Pcgf1* and *Pcgf6* single matKO, respectively. **h, i, j**, The numbers of implantation (**h**), the litter sizes (**i**) and the placental weights (**j**) of the indicated matKO embryos. The numbers of litters and placentae examined are 11 and 85 (CTR), 10 and 24 (*Pcgf1/6* matKO), 7 and 48 (*Pcgf1* matKO), and 10 and 69 (*Pcgf6* matKO), respectively. Bars overlaid on the plots indicate mean ± SD. ***$p < 0.0001$ (two-tailed Student's *t*-test).

nature research

Corresponding author(s): Azusa Inoue

Last updated by author(s): Feb 12, 2021

Reporting Summary

Nature Research wishes to improve the reproducibility of the work that we publish. This form provides structure for consistency and transparency in reporting. For further information on Nature Research policies, see our Editorial Policies and the Editorial Policy Checklist.

Statistics

For all statistical analyses, confirm that the following items are present in the figure legend, table legend, main text, or Methods section.

n/a	Confirmed	
☐	☒	The exact sample size (*n*) for each experimental group/condition, given as a discrete number and unit of measurement
☐	☒	A statement on whether measurements were taken from distinct samples or whether the same sample was measured repeatedly
☐	☒	The statistical test(s) used AND whether they are one- or two-sided *Only common tests should be described solely by name; describe more complex techniques in the Methods section.*
☒	☐	A description of all covariates tested
☐	☒	A description of any assumptions or corrections, such as tests of normality and adjustment for multiple comparisons
☐	☒	A full description of the statistical parameters including central tendency (e.g. means) or other basic estimates (e.g. regression coefficient) AND variation (e.g. standard deviation) or associated estimates of uncertainty (e.g. confidence intervals)
☐	☒	For null hypothesis testing, the test statistic (e.g. *F*, *t*, *r*) with confidence intervals, effect sizes, degrees of freedom and *P* value noted *Give P values as exact values whenever suitable.*
☒	☐	For Bayesian analysis, information on the choice of priors and Markov chain Monte Carlo settings
☒	☐	For hierarchical and complex designs, identification of the appropriate level for tests and full reporting of outcomes
☐	☒	Estimates of effect sizes (e.g. Cohen's *d*, Pearson's *r*), indicating how they were calculated

Our web collection on statistics for biologists contains articles on many of the points above.

Software and code

Policy information about availability of computer code

Data collection	Data was collected by Illumina's software installed on Illumina NextSeq 500 (bcl2fastq v2.17 and RTA v2.4.11).
Data analysis	Trim Galore v0.6.4 Bowtie2 v2.3.5 Sambamba 0.7.1 samtools v1.7 deepTools2 v3.3.1 SNPsplit v0.3.4 MACS2 v2.1.2 BEDtools v2.26.0 STAR v2.7.3 RSEM v1.3.1 featureCounts v1.6.0 cutadapt v2.8 edgeR v3.28.0 ChIPseeker v1.22.1 GeneOverlap v1.23.0 R v3.6.2 sratoolkit v2.10.0 Integrative Genomics Viewer v2.8.0

For manuscripts utilizing custom algorithms or software that are central to the research but not yet described in published literature, software must be made available to editors and reviewers. We strongly encourage code deposition in a community repository (e.g. GitHub). See the Nature Research guidelines for submitting code & software for further information.

Data

Policy information about availability of data

All manuscripts must include a data availability statement. This statement should provide the following information, where applicable:

- Accession codes, unique identifiers, or web links for publicly available datasets
- A list of figures that have associated raw data
- A description of any restrictions on data availability

The statistics of datasets generated in this study are summarized in Tables S6. The H2AK119ub1 ChIP-seq datasets of mESCs were from GSE119620. H3K27me3 and H3K4me3 ChIP-seq and WGBS datasets of FGOs were from GSE93941. H3K27me3 ChIP-seq datasets of 7d-GOs, MII oocytes, zygotes, early 2-cell, late 2-cell, ICM of blastocysts, and E6.5 epiblast were from GSE76687. H3K27me3 CUT&RUN datasets of morula embryos were from GSE116713. H3K27me3 ChIP-seq datasets in mESCs were from GSE119620. RNA-seq datasets of Ring1a/1b KO FGOs, Dnmt3l matKO and Eed matKO morula embryos were from GSE132156, GSE130115 and GSE116713, respectively. PCGF1 ChIP-seq datasets in mESCs were from GSE119620. Raw and processed CUT&RUN and RNA-seq data have been deposited in the Gene Expression Omnibus (GEO) database under accession number GSE153496. https://www.ncbi.nlm.nih.gov/geo/query/acc.cgi?acc=GSE153496

Field-specific reporting

Please select the one below that is the best fit for your research. If you are not sure, read the appropriate sections before making your selection.

☒ Life sciences ☐ Behavioural & social sciences ☐ Ecological, evolutionary & environmental sciences

For a reference copy of the document with all sections, see nature.com/documents/nr-reporting-summary-flat.pdf

Life sciences study design

All studies must disclose on these points even when the disclosure is negative.

Sample size	Sample sizes were determined based on the standard of this field.
Data exclusions	Duplicated reads or multiple mapped reads were excluded from CUT&RUN analysis.
Replication	CUT&RUN and RNA-seq were performed in duplicate or triplicate (written in the figure legends). The correlation coefficiency between replicates were shown in the supplementary data The unique reads were pooled to analyze the data after confirmation of the reproducibility.
Randomization	Not relevant because most comparisons were done between WT and mutants.
Blinding	Not blinded during sample collection or analysis, as the genotype information is critical for the experiment and analysis.

Reporting for specific materials, systems and methods

We require information from authors about some types of materials, experimental systems and methods used in many studies. Here, indicate whether each material, system or method listed is relevant to your study. If you are not sure if a list item applies to your research, read the appropriate section before selecting a response.

Materials & experimental systems

n/a	Involved in the study
☐	☒ Antibodies
☐	☒ Eukaryotic cell lines
☒	☐ Palaeontology and archaeology
☐	☒ Animals and other organisms
☒	☐ Human research participants
☒	☐ Clinical data
☒	☐ Dual use research of concern

Methods

n/a	Involved in the study
☐	☒ ChIP-seq
☒	☐ Flow cytometry
☒	☐ MRI-based neuroimaging

Antibodies

Antibodies used

CUT&RUN
H2AK119ub1 (Cell Signaling Technology, #8240, Lot 2)
H3K27me3 antibody (Diagenode, #C15410069, Lot D1820D)
Immunofluorecence
H2AK119ub1 (Cell Signaling Technology, #8240)
H3K27me3 (Active Motif, #61017)
H3K27me3 (Merck Millipore, #07-449)
Oct3/4 (Santa Cruz #sc-8628)

H3.3 (Abnova H00003021-M01)
Alexa Flour 488 donkey anti-mouse IgG(Life technologies)
Alexa Flour 568 donkey anti-rabbit IgG (Life technologies)
Alexa Flour 647 donkey anti-goat IgG (Life technologies)

Validation

The specificity of the H2AK119ub1 antibody for IF was validated by Zheng et al., 2020 Mol Cell (referred in this manuscript) that studied Ring1a/1b KO oocytes. We also validated it by studying Pcgf1/6 KO oocytes in both IF and CUT&RUN.
The specificity of the H3K27me3 antibodies for both IF (Active motif and Merck Millipore) and CUT&RUN (Diagenode) were validated by Inoue et al., 2018 Genes Dev (referred in this manuscript) that studied Eed KO oocytes and maternal KO embryos.
The specificity of the H3.3 antibody was validated in the commercial website (http://www.abnova.com/products/products_detail.asp?catalog_id=H00003021-M01).
The specificity of the Oct3/4 antibody was validated in Cell, 165 (2016) 1375-1388. doi:10.1016/j.cell.2016.05.050

Eukaryotic cell lines

Policy information about cell lines

Cell line source(s)

State the source of each cell line used.

Authentication

Describe the authentication procedures for each cell line used OR declare that none of the cell lines used were authenticated.

Mycoplasma contamination

Confirm that all cell lines tested negative for mycoplasma contamination OR describe the results of the testing for mycoplasma contamination OR declare that the cell lines were not tested for mycoplasma contamination.

Commonly misidentified lines
(See ICLAC register)

Name any commonly misidentified cell lines used in the study and provide a rationale for their use.

Animals and other organisms

Policy information about studies involving animals; ARRIVE guidelines recommended for reporting animal research

Laboratory animals

C57/BL6N (4-10 week-old females and postnatal day 7 females)
PWK/PhJ (3-6 month-old males)
B6D2F1 (2-6 month-old males)
The Pcgf1flox mouse line was established previously (ref45). The Pcgf6flox mouse line was generated from a Pcgf6flox ESC line that was previously described (ref63). The ESCs were aggregated with 8-cell stage embryos to generate chimeric mice that were then mated with B6;SJL-Tg(ACTFLPe)9025Dym/J mice (Jackson Laboratory, 003800) to remove the neomycin resistance gene cassette. Both mouse lines are on a B6/129 mixed background. The Pcgf1flox and Pcgf6flox females were crossed with a Zp3Cre mouse line [Jackson Laboratory, C57BL/6-Tg(Zp3-cre)93Knw/J, 003651] to obtain Zp3Cre/Pcgf1flox/flox/Pcgf6flox/flox males and Pcgf1flox/flox/Pcgf6flox/flox females. They were intercrossed to obtain Pcgf1flox/flox/Pcgf6flox/flox (CTR) and Zp3Cre/Pcgf1flox/flox/Pcgf6flox/flox (double KO) females for our experiments. The respective single KO females, Zp3Cre/Pcgf1flox/flox/Pcgf6+/+ or +/flox (Pcgf1 single KO) and Zp3Cre/Pcgf1+/+ or +/flox/Pcgf6flox/flox (Pcgf6 single KO), were obtained by backcrossing the Zp3Cre/Pcgf1flox/flox/Pcgf6flox/flox males with B6N followed by intercrossing. Double heterozygous males were obtained by crossing the double KO females and B6N males. These females were used at 4-12 week-old to collect oocytes and at 8-12 week-old for natural mating experiments.

Wild animals

This study did not involve wild animals.

Field-collected samples

This study did not involve samples collected from the field.

Ethics oversight

All animal experiments were performed in accordance with guidelines of the Institutional Animal Care and Use Committee at RIKEN Center for Integrative Medical Sciences.

Note that full information on the approval of the study protocol must also be provided in the manuscript.

ChIP-seq

Data deposition

☒ Confirm that both raw and final processed data have been deposited in a public database such as GEO.

☒ Confirm that you have deposited or provided access to graph files (e.g. BED files) for the called peaks.

Data access links
May remain private before publication.

https://www.ncbi.nlm.nih.gov/geo/query/acc.cgi?acc=GSE153496

Files in database submission

CUT&RUN raw data:
GSM4645212 -- H2AK119ub1_7d_oocyte_rep1.fastq.gz
GSM4645213 -- H2AK119ub1_7d_oocyte_rep2.fastq.gz
GSM4645214 -- H2AK119ub1_FGO_oocyte_rep1.fastq.gz
GSM4645215 -- H2AK119ub1_FGO_oocyte_rep2.fastq.gz
GSM4645216 -- H2AK119ub1_MII_oocyte_rep1.fastq.gz
GSM4645217 -- H2AK119ub1_MII_oocyte_rep2.fastq.gz
GSM4645218 -- H2AK119ub1_1_cell_rep1.fastq.gz

GSM4645219 -- H2AK119ub1_1_cell_rep2.fastq.gz
GSM4645220 -- H2AK119ub1_early_2_cell_rep1.fastq.gz
GSM4645221 -- H2AK119ub1_early_2_cell_rep2.fastq.gz
GSM4645222 -- H2AK119ub1_late_2_cell_rep1.fastq.gz
GSM4645223 -- H2AK119ub1_late_2_cell_rep2.fastq.gz
GSM4645224 -- H2AK119ub1_morula_rep1.fastq.gz
GSM4645225 -- H2AK119ub1_morula_rep2.fastq.gz
GSM4645226 -- H2AK119ub1_blastocyst_rep1.fastq.gz
GSM4645227 -- H2AK119ub1_blastocyst_rep2.fastq.gz
GSM4645228 -- H2AK119ub1_mESC_250_cells.fastq.gz
GSM4645229 -- H2AK119ub1_mESC_500_cells.fastq.gz
GSM4645230 -- H2AK119ub1_mESC_1k_cells.fastq.gz
GSM4645231 -- H2AK119ub1_mESC_5k_cells.fastq.gz
GSM4645232 -- H2AK119ub1_FGO_Pcgf1/6_CTR_rep1.fastq.gz
GSM4645233 -- H2AK119ub1_FGO_Pcgf1/6_CTR_spike-in_rep2.fastq.gz
GSM4645234 -- H2AK119ub1_FGO_Pcgf1/6_KO_rep1.fastq.gz
GSM4645235 -- H2AK119ub1_FGO_Pcgf1/6_KO_spike-in_rep2.fastq.gz
GSM4645236 -- H3K27me3_FGO_Pcgf1/6_CTR_rep1.fastq.gz
GSM4645237 -- H3K27me3_FGO_Pcgf1/6_CTR_rep2.fastq.gz
GSM4645238 -- H3K27me3_FGO_Pcgf1/6_KO_rep1.fastq.gz
GSM4645239 -- H3K27me3_FGO_Pcgf1/6_KO_rep2.fastq.gz
GSM4645240 -- H3K27me3_morula_Pcgf1/6_CTR_rep1.fastq.gz
GSM4645241 -- H3K27me3_morula_Pcgf1/6_CTR_rep2.fastq.gz
GSM4645242 -- H3K27me3_morula_Pcgf1/6_CTR_rep3.fastq.gz
GSM4645243 -- H3K27me3_morula_Pcgf1/6_matKO_rep1.fastq.gz
GSM4645244 -- H3K27me3_morula_Pcgf1/6_matKO_rep2.fastq.gz
GSM4645245 -- H3K27me3_morula_Pcgf1/6_matKO_rep3.fastq.gz
GSM4916276 -- H3K27me3_FGO_Pcgf1_KO_rep1.fastq.gz
GSM4916277 -- H3K27me3_FGO_Pcgf1_KO_rep2.fastq.gz
GSM4916278 -- H3K27me3_FGO_Pcgf6_KO_rep1.fastq.gz
GSM4916279 -- H3K27me3_FGO_Pcgf6_KO_rep2.fastq.gz
GSM4916280 -- H3K27me3_late_2_cell_Pcgf1/6_CTR_rep1.fastq.gz
GSM4916281 -- H3K27me3_late_2_cell_Pcgf1/6_matKO_rep1.fastq.gz
CUT&RUN processed data:
H2AK119ub1_7d_oocyte_merge_replicates_maternal.bigwig
H2AK119ub1_FGO_oocyte_merge_replicates_maternal.bigwig
H2AK119ub1_MII_oocyte_merge_replicates_maternal.bigwig
H2AK119ub1_1_cell_merge_replicates_maternal.bigwig
H2AK119ub1_1_cell_merge_replicates_paternal.bigwig
H2AK119ub1_early_2_cell_merge_replicates_maternal.bigwig
H2AK119ub1_early_2_cell_merge_replicates_paternal.bigwig
H2AK119ub1_late_2_cell_merge_replicates_maternal.bigwig
H2AK119ub1_late_2_cell_merge_replicates_paternal.bigwig
H2AK119ub1_morula_merge_replicates_maternal.bigwig
H2AK119ub1_morula_merge_replicates_paternal.bigwig
H2AK119ub1_blastocyst_merge_replicates_maternal.bigwig
H2AK119ub1_blastocyst_merge_replicates_paternal.bigwig
H2AK119ub1_mESC_pool_samples.bigwig
H3K27me3_morula_Pcgf1.6_CTR_merge_replicates_maternal.bigwig
H3K27me3_morula_Pcgf1.6_CTR_merge_replicates_paternal.bigwig
H3K27me3_morula_Pcgf1.6_matKO_merge_replicates_maternal.bigwig
H3K27me3_morula_Pcgf1.6_matKO_merge_replicates_paternal.bigwig
H2AK119ub1_7d_oocyte_rep1_unique.bigwig
H2AK119ub1_7d_oocyte_rep2_unique.bigwig
H2AK119ub1_FGO_oocyte_rep1_unique.bigwig
H2AK119ub1_FGO_oocyte_rep2_unique.bigwig
H2AK119ub1_MII_oocyte_rep1_unique.bigwig
H2AK119ub1_MII_oocyte_rep2_unique.bigwig
H2AK119ub1_mESC_250_cells_unique.bigwig
H2AK119ub1_mESC_500_cells_unique.bigwig
H2AK119ub1_mESC_1K_cells_unique.bigwig
H2AK119ub1_mESC_5K_cells_unique.bigwig
H2AK119ub1_FGO_Pcgf1.6_CTR_rep1_unique.bigwig
H2AK119ub1_FGO_Pcgf1.6_CTR_spike_in_rep2_unique.bigwig
H2AK119ub1_FGO_Pcgf1.6_KO_rep1_unique.bigwig
H2AK119ub1_FGO_Pcgf1.6_KO_spike_in_rep2_unique.bigwig
H3K27me3_FGO_Pcgf1.6_CTR_rep1_unique.bigwig
H3K27me3_FGO_Pcgf1.6_CTR_rep2_unique.bigwig
H3K27me3_FGO_Pcgf1.6_KO_rep1_unique.bigwig
H3K27me3_FGO_Pcgf1.6_KO_rep2_unique.bigwig
H3K27me3_morula_Pcgf1.6_CTR_rep1_unique.bigwig
H3K27me3_morula_Pcgf1.6_CTR_rep2_unique.bigwig
H3K27me3_morula_Pcgf1.6_CTR_rep3_unique.bigwig
H3K27me3_morula_Pcgf1.6_matKO_rep1_unique.bigwig
H3K27me3_morula_Pcgf1.6_matKO_rep2_unique.bigwig
H3K27me3_morula_Pcgf1.6_matKO_rep3_unique.bigwig

H3K27me3_late_2_cell_Pcgf1.6_CTR_scaled.bigwig
H3K27me3_late_2_cell_Pcgf1.6_CTR_paternal.bigwig
H3K27me3_late_2_cell_Pcgf1.6_CTR_maternal.bigwig
H3K27me3_late_2_cell_Pcgf1.6_matKO_scaled.bigwig
H3K27me3_late_2_cell_Pcgf1.6_matKO_paternal.bigwig
H3K27me3_late_2_cell_Pcgf1.6_matKO_maternal.bigwig
RNA-seq raw data:
GSM4645246 -- RNA-seq_FGO_Pcgf1/6_CTR_rep1.fastq.gz
GSM4645247 -- RNA-seq_FGO_Pcgf1/6_CTR_rep2.fastq.gz
GSM4645248 -- RNA-seq_FGO_Pcgf1/6_KO_rep1.fastq.gz
GSM4645249 -- RNA-seq_FGO_Pcgf1/6_KO_rep2.fastq.gz
GSM4645250 -- RNA-seq_morula_Pcgf1/6_CTR_rep1.fastq.gz
GSM4645251 -- RNA-seq_morula_Pcgf1/6_CTR_rep2.fastq.gz
GSM4645252 -- RNA-seq_morula_Pcgf1/6_matKO_rep1.fastq.gz
GSM4645253 -- RNA-seq_morula_Pcgf1/6_matKO_rep2.fastq.gz
GSM4645254 -- RNA-seq_morula_B6xPWK_rep1.fastq.gz
GSM4645255 -- RNA-seq_morula_B6xPWK_rep2.fastq.gz
GSM4645256 -- RNA-seq_morula_PWKxB6_rep1.fastq.gz
GSM4645257 -- RNA-seq_morula_PWKxB6_rep2.fastq.gz
GSM4645258 -- RNA-seq_ExE_Pcgf1/6_CTR_rep1.fastq.gz
GSM4645259 -- RNA-seq_ExE_Pcgf1/6_CTR_rep2.fastq.gz
GSM4645260 -- RNA-seq_ExE_Pcgf1/6_matKO_rep1.fastq.gz
GSM4645261 -- RNA-seq_ExE_Pcgf1/6_matKO_rep2.fastq.gz
GSM4645262 -- RNA-seq_ExE_Pcgf1/6_matKO_rep3.fastq.gz
GSM4645263 -- RNA-seq_ExE_Pcgf1/6_matKO_rep4.fastq.gz
RNA-seq processed data:
RNA_seq_gene_counts_matrix.txt

Genome browser session
(e.g. UCSC)

N.A.

Methodology

Replicates

Duplicate in most samples. Triplicate in a certain sample. The correlation between replicates was shown in the manuscript.

Sequencing depth

Detail information was provided in Table S7.

Samples Raw_reads Unique_and_non-redundant_reads
H2AK119ub1_7d_oocyte_rep1.fastq.gz 36,662,623 19,950,734
H2AK119ub1_7d_oocyte_rep2.fastq.gz 35,369,905 17,506,515
H2AK119ub1_FGO_oocyte_rep1.fastq.gz 58,516,193 18,366,459
H2AK119ub1_FGO_oocyte_rep2.fastq.gz 44,933,107 23,135,306
H2AK119ub1_MII_oocyte_rep1.fastq.gz 44,633,586 14,374,555
H2AK119ub1_MII_oocyte_rep2.fastq.gz 26,985,604 11,065,606
H2AK119ub1_1_cell_rep1.fastq.gz 62,421,144 15,367,715
H2AK119ub1_1_cell_rep2.fastq.gz 43,612,425 21,777,164
H2AK119ub1_early_2_cell_rep1.fastq.gz 35,457,213 23,605,837
H2AK119ub1_early_2_cell_rep2.fastq.gz 61,690,155 21,038,163
H2AK119ub1_late_2_cell_rep1.fastq.gz 45,065,423 17,757,579
H2AK119ub1_late_2_cell_rep1.fastq.gz 51,561,320 24,527,538
H2AK119ub1_morula_rep1.fastq.gz 50,795,637 24,328,768
H2AK119ub1_morula_rep1.fastq.gz 34,616,124 24,069,057
H2AK119ub1_blastocyst_rep1.fastq.gz 35,852,621 18,801,757
H2AK119ub1_blastocyst_rep2.fastq.gz 44,999,877 30,426,937
H2AK119ub1_mESC_250_cells.fastq.gz 27,585,321 2,187,919
H2AK119ub1_mESC_500_cells.fastq.gz 24,727,868 12,242,472
H2AK119ub1_mESC_1k_cells.fastq.gz 13,918,446 8,398,094
H2AK119ub1_mESC_5k_cells.fastq.gz 22,713,145 10,471,754
H2AK119ub1_FGO_Pcgf1/6_CTR_rep1.fastq.gz 58,323,051 14,795,344
H2AK119ub1_FGO_Pcgf1/6_CTR_spike-in_rep2.fastq.gz 62,651,746 39,459,857
H2AK119ub1_FGO_Pcgf1/6_KO_rep1.fastq.gz 23,065,628 2,457,355
H2AK119ub1_FGO_Pcgf1/6_KO_spike-in_rep2.fastq.gz 63,614,590 30,372,613
H3K27me3_FGO_Pcgf1/6_CTR_rep1.fastq.gz 41,516,026 25,237,194
H3K27me3_FGO_Pcgf1/6_CTR_rep2.fastq.gz 38,098,837 25,421,712
H3K27me3_FGO_Pcgf1/6_KO_rep1.fastq.gz 33,515,846 18,455,232
H3K27me3_FGO_Pcgf1/6_KO_rep2.fastq.gz 35,253,635 20,690,384
H3K27me3_morula_Pcgf1/6_CTR_rep1.fastq.gz 38,840,904 17,554,389
H3K27me3_morula_Pcgf1/6_CTR_rep2.fastq.gz 57,994,160 9,627,573
H3K27me3_morula_Pcgf1/6_CTR_rep3.fastq.gz 35,507,948 21,913,231
H3K27me3_morula_Pcgf1/6_matKO_rep1.fastq.gz 33,100,011 15,247,854
H3K27me3_morula_Pcgf1/6_matKO_rep2.fastq.gz 49,440,994 16,714,968
H3K27me3_morula_Pcgf1/6_matKO_rep3.fastq.gz 41,708,682 27,279,918
RNA-seq_FGO_Pcgf1/6_CTR_rep1.fastq.gz 41,468,185 33,104,826
RNA-seq_FGO_Pcgf1/6_CTR_rep2.fastq.gz 39,331,346 31,640,760
RNA-seq_FGO_Pcgf1/6_KO_rep1.fastq.gz 35,663,517 27,679,249
RNA-seq_FGO_Pcgf1/6_KO_rep2.fastq.gz 29,461,919 23,873,580

RNA-seq_morula_Pcgf1/6_CTR_rep1.fastq.gz 81,253,316 52,757,454
RNA-seq_morula_Pcgf1/6_CTR_rep2.fastq.gz 74,410,359 48,854,430
RNA-seq_morula_Pcgf1/6_matKO_rep1.fastq.gz 73,383,743 40,996,444
RNA-seq_morula_Pcgf1/6_matKO_rep2.fastq.gz 67,215,203 41,151,017
RNA-seq_morula_B6xPWK_rep1.fastq.gz 63,150,715 42,571,025
RNA-seq_morula_B6xPWK_rep2.fastq.gz 51,012,496 34,430,170
RNA-seq_morula_PWKxB6_rep1.fastq.gz 132,481,007 90,522,738
RNA-seq_morula_PWKxB6_rep2.fastq.gz 85,809,247 55,925,011
RNA-seq_ExE_Pcgf1/6_CTR_rep1.fastq.gz 44,704,667 32,808,578
RNA-seq_ExE_Pcgf1/6_CTR_rep2.fastq.gz 46,425,457 33,644,463
RNA-seq_ExE_Pcgf1/6_matKO_rep1.fastq.gz 44,622,443 32,483,183
RNA-seq_ExE_Pcgf1/6_matKO_rep2.fastq.gz 43,308,188 31,174,188
RNA-seq_ExE_Pcgf1/6_matKO_rep3.fastq.gz 40,894,540 29,246,713
RNA-seq_ExE_Pcgf1/6_matKO_rep4.fastq.gz 37,352,077 26,862,644

Antibodies

H2AK119ub1 (Cell Signaling Technology, #8240, Lot 2)
H3K27me3 antibody (Diagenode, #C15410069, Lot D1820D)

Peak calling parameters

MACS2 (version 2.1.2) was used for peak calling with the parameters "-g mm --nomodel --nolambda --broad". H2AK119ub1 and H3K27me3 peaks with distance shorter than 5 kb were merged using the merge function from BEDtools (version 2.26.0) for downstream analysis. Peaks identified in all biological replicates were combined and used for further analysis.

Data quality

To validate the quality of CUT&RUN, We confirmed that all of the H2AK119ub1 CUT&RUN datasets using 250, 500, 1,000, and 5,000 mouse ESCs (mESCs) are highly correlated with a public H2AK119ub1 ChIP-seq dataset (Spearman's correlation coefficient: 0.82-0.89).

Software

Trim Galore v0.6.4
Bowtie2 v2.3.5
Sambamba 0.7.1
samtools v1.7
deepTools2 v3.3.1
SNPsplit v0.3.4
MACS2 v2.1.2
BEDtools v2.26.0
cutadapt v2.8
ChIPseeker v1.22.1
GeneOverlap v1.23.0